



HAL
open science

Characterization of an RF-driven argon plasma at atmospheric pressure using broadband absorption and optical emission spectroscopy

G. Nayak, M. Simeni Simeni, J. Rosato, N. Sadeghi, P. Bruggeman

► **To cite this version:**

G. Nayak, M. Simeni Simeni, J. Rosato, N. Sadeghi, P. Bruggeman. Characterization of an RF-driven argon plasma at atmospheric pressure using broadband absorption and optical emission spectroscopy. *Journal of Applied Physics*, 2020, 128 (24), pp.243302. 10.1063/5.0035488 . hal-03215642

HAL Id: hal-03215642

<https://hal.science/hal-03215642>

Submitted on 11 May 2021

HAL is a multi-disciplinary open access archive for the deposit and dissemination of scientific research documents, whether they are published or not. The documents may come from teaching and research institutions in France or abroad, or from public or private research centers.

L'archive ouverte pluridisciplinaire **HAL**, est destinée au dépôt et à la diffusion de documents scientifiques de niveau recherche, publiés ou non, émanant des établissements d'enseignement et de recherche français ou étrangers, des laboratoires publics ou privés.

Characterization of an RF-driven argon plasma at atmospheric pressure using broadband absorption and optical emission spectroscopy

G. Nayak,^{1, a)} M. Simeni Simeni,¹ J. Rosato,² N. Sadeghi,^{3, b)} and P. J. Bruggeman^{1, c)}

¹⁾*Department of Mechanical Engineering, University of Minnesota, Minneapolis, Minnesota 55455, USA*

²⁾*Aix-Marseille Université, CNRS, PIIM UMR7345, 13397 Marseille, France*

³⁾*LIPhy (URA5588) & LTM (URA5129), Université Grenoble-Alpes & CNRS, Grenoble, France*

(Dated: 30 November 2020)

Atmospheric pressure plasmas in argon are of particular interest due to the production of highly excited and reactive species enabling numerous plasma-aided applications. In this contribution, we report on absolute optical emission and absorption spectroscopy of a radio frequency (RF) driven capacitively coupled argon glow discharge operated in a parallel-plate configuration. This enabled the study of all key parameters including electron density and temperature, gas temperature, and absolute densities of atoms in highly electronically excited states. The space and time-averaged electron density and temperature were determined from the measurement of the absolute intensity of the electron-atom bremsstrahlung in the visible range. Considering the non-Maxwellian electron energy distribution function, an electron temperature (T_e) of 2.1 eV and an electron density (n_e) of $1.1 \times 10^{19} \text{ m}^{-3}$ were obtained. The time-averaged and spatially resolved absolute densities of atoms in the metastable ($1s_5$ and $1s_3$) and resonant ($1s_4$ and $1s_2$) states of argon in pure Ar and Ar/He mixture were obtained by broadband absorption spectroscopy. The $1s_5$ metastable atoms had the largest density near the sheath region with a maximum value of $8 \times 10^{17} \text{ m}^{-3}$, while all other $1s$ states had densities of at most $2 \times 10^{17} \text{ m}^{-3}$. The dominant production and loss mechanisms of these atoms were discussed, in particular, the role of radiation trapping. We conclude with a comparison of the plasma properties of the argon RF glow discharges with the more common He equivalent and highlight their differences.

I. INTRODUCTION

Plasmas operating at atmospheric pressure in argon have witnessed a tremendous growth in last few decades. The non-equilibrium feature of such discharges allows production of highly excited and reactive species initiated by energetic electrons, which have enabled a plethora of applications, including gas discharge laser systems such as optically pumped rare gas lasers (OPRGLs) operated in Ar/He mixtures,^{1–5} gas discharge lamps, plasma medicine,^{6–8} surface modification,^{9–11} and surface decontamination.^{12–14} In highly repetitive discharges, such as radio frequency (RF) driven plasmas, the long-lived charged and energetic species from the previous discharge cycle enable to sustain stable discharges at lower voltage requirements. The argon metastable species are one of those strong contenders for driving the kinetics in these low temperature plasmas.¹⁵ Due to their relatively long lifetime, atoms in the metastable states are known to be excellent reservoirs of energy. The excitation energy required for metastable production (11.6 eV) is lower than the ionization energy of argon (15.8 eV). Thus, these metastable atoms can be produced efficiently and can further lead to ionization at lower electron energy via stepwise ionization.

Since argon is used as a feed gas for many plasma-aided applications, it becomes imperative to study its metastable states in terms of the absolute densities and the spatial distribution within the active plasma region. Numerous mod-

eling studies have been carried out to understand the kinetics of the argon metastable atoms in Ar and Ar/He plasmas over a wide range of pressures (few mTorr to atmospheric pressure).^{2, 16–20} However, only a handful of papers report measurements of these vital species at atmospheric pressure. Most of the argon metastable species measurements are performed using tunable diode laser absorption spectroscopy^{4, 5, 21–25} or time-resolved laser induced fluorescence measurements.¹ In addition, the resonant states of argon could also be important energy reservoirs, but they have only been studied in low pressure argon plasmas.^{26–28} At atmospheric pressure, the effective lifetimes of the metastable states of Ar, $1s_5$ and $1s_3$ (Paschen's notation, details provided further in Table II), are governed by three-body collisions with two ground state Ar atoms, producing Ar_2^* excimers, and by collisional transfer to the resonant states, $1s_2$ and $1s_4$ via both electron-impact and heavy particle collisions.^{28, 29} A more detailed measurement/analysis of the population of these resonant states will facilitate an understanding of the dominant energy transfer mechanism(s) and its potential impact on plasma kinetics.

In this work, the time-averaged absolute densities of Ar atoms in both metastable and resonant states of Ar in pure Ar and Ar/He gas mixtures in an RF-driven capacitively coupled glow discharge at atmospheric pressure are measured using broadband absorption spectroscopy. The electron temperature and density are determined from continuum radiation emission spectroscopy and compared with the electron density obtained from a previously reported electrical impedance measurement approach.³⁰ The experimental setup, optical diagnostics and a detailed procedure to determine the electron temperature and density as well as the absolute densities from

^{a)}Electronic mail: nayak025@umn.edu

^{b)}Electronic mail: nader.sadeghi@univ-grenoble-alpes.fr

^{c)}Electronic mail: pbruggem@umn.edu

the measured absorption data are described before we present the results. The estimated electron properties and the spatially distributed densities of atoms in the metastable and resonant states of Ar across the plasma gap allow to discuss the production and destruction mechanisms of the excited atoms of Ar in detail.

II. METHODS

A. Experimental setup

A schematic of the experimental setup is shown in Fig. 1(a). The plasma reactor used in this study generates an RF-driven capacitively coupled glow discharge in a water-cooled parallel plate electrode type configuration. A detailed description of the reactor is provided in^{31,32}. The reactor is designed to facilitate access for optical diagnostics along the length of the plasma (19.1 mm) and within the inter-electrode spacing of 2 mm. The discharge was generated at atmospheric pressure in argon (ultra-pure carrier grade 99.999%) as well as in helium (ultra-pure carrier grade 99.9995%) with 17% admixture of argon to elucidate on the effect of absolute densities of atoms in the metastable and resonant states of Ar with He as the perturber atom. The total flow rate of the gas or gas mixture used was maintained using electronic mass flow controllers (MFCs) at 1 standard liter per minute (slm) for Ar and He + 17% Ar plasmas. The time-averaged plasma images for different gas conditions were obtained using a digital camera with a 1/10s exposure time.

The RF power (13.56 MHz) was applied continuously and only time-averaged densities of metastable and resonant atoms are reported. The discharge power was determined by acquiring and recording voltage and current data on a digital oscilloscope (Tektronix DPO2024B, 200 MHz, 1 Gs⁻¹) using a voltage probe (Tektronix P5100A) and a Rogowski coil (Pearson Electronics, Model 2878), respectively as shown in Fig. 1(a). The discharge powers used for different gas mixture are reported in Table I.

B. Spectroscopy of emission continuum

The continuum radiation, visible in pure Ar discharge (Fig. 1(b)), mostly originates from collision-induced processes, for example, free-free bremsstrahlung and free-bound recombination between electrons and ions in low pressure plasmas.³³ However, in weakly ionized plasmas with a low degree of ionization ($n_e/n_a < 10^{-4}$, n_a being the density of the neutral atom), such as the atmospheric pressure glow discharges studied in this work, the continuum radiation emitted through interactions between free electrons and neutral atoms becomes dominant over the electron-ion interactions typical for high density plasmas, where Coulomb collisions dominate.³⁴ This ‘‘continuum’’ radiation is further composed of two major contributing mechanisms: (a) the electron-neutral atom (e - a) or neutral bremsstrahlung, caused by the deceleration of a free electron during its interaction with a

TABLE I. Discharge power for different plasma conditions.

Gas	Flow rate (slm)	Power (W)
Ar	1	13.5 ± 0.2
He	1	14.0 ± 0.5
He + 17% Ar	1	12.4 ± 1.4

neutral atom, and (b) the polarization bremsstrahlung, which originates from the time-dependent induced dipole moment in neutral atom by the Coulomb field of the incident electron. However, it is shown that for electron-argon collisions with $T_e > 0.9$ eV, the neutral bremsstrahlung spectral intensities are much higher than that of polarization bremsstrahlung.³⁵ This was further confirmed by numerical studies in³⁶, which showed that the induced dipole radiation contributes to < 8% of the total radiation for a $T_e = 0.5$ eV, and was insignificant in most cases. Thus, in this study, the continuum radiation will be analyzed and discussed based on neutral bremsstrahlung only.

The emission from the continuum radiation is usually studied by determining the emissivity as function of wavelength. The emissivity of the e - a bremsstrahlung has been reported in detail in³⁷ and can be expressed as

$$\epsilon_{ea} = 4\pi \times \sqrt{\frac{2}{m_e}} \frac{n_e n_a}{\lambda^2} \frac{hc}{4\pi} \int_{hv}^{\infty} \sigma_{ea}^B(\lambda, E) \sqrt{E} f(E) dE, \quad (1)$$

where m_e , λ , h , c , hv and E are the mass of an electron, the wavelength of the emitted photon, the Planck constant, the speed of light in vacuum, the energy of the emitted photon and the energy of the electron, respectively. In this work, we use SI units and ϵ_{ea} has the units [W m⁻³ nm⁻¹]. The electron energy distribution function (EEDF), $f(E)$ is derived from Bolsig+³⁸ and both Maxwellian as well as non-Maxwellian distributions are considered to compare their effect on the estimation of T_e and n_e . The neutral bremsstrahlung cross-section $\sigma_{ea}^B(\lambda, E)$ according to³⁹ is given by

$$\sigma_{ea}^B(\lambda, E) = \frac{8\alpha}{3\pi} \frac{E}{m_e c^2} \left(1 - \frac{hc}{2\lambda E}\right) \sqrt{1 - \frac{hc}{\lambda E}} \sigma_{ea}^{\text{mom}}(E), \quad (2)$$

where $\sigma_{ea}^{\text{mom}}(E)$ is the cross-section for momentum transfer between the electron and the neutral argon atom adopted from the Phelps database in LXCat.^{38,40} The fine structure constant α is given by

$$\alpha = \frac{e^2}{2\epsilon_0 hc}. \quad (3)$$

Substituting Eq. 2 in Eq. 1 yields

$$\epsilon_{ea} = C_{ea} \frac{n_e n_a}{\lambda^2} \int_{hv}^{\infty} \sigma_{ea}^{\text{mom}}(E) E^{3/2} \times \left(1 - \frac{hc}{2\lambda E}\right) \sqrt{1 - \frac{hc}{\lambda E}} f(E) dE, \quad (4)$$

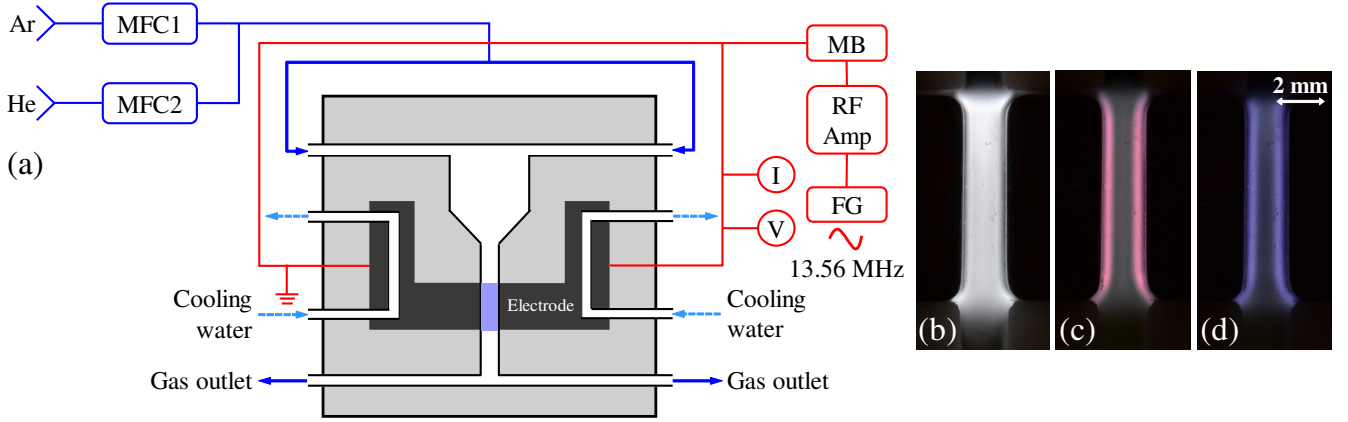


FIG. 1. (a) Experimental schematic of the plasma reactor, and digital color images of the plasma operated in (b) pure Ar, (c) pure He, and (d) He + 17% Ar. (FG: function generator, RF Amp: RF amplifier, MB: matching box, MFC: mass flow controller)

where $C_{ea} = (2\sqrt{2}/3\pi^2)(\alpha h/m_e^{3/2}c) = 1.77$ [$\text{W m}^2 \text{J}^{-3/2} \text{sr}^{-1}$]. The EEDF, $f(E)$ has units [$\text{eV}^{-3/2}$]. Integrating $E^{-1/2}f(E)$ over the entire energy range yields 1. Eq. 4 shows that T_e and n_e determine the spectral shape and the intensity of the neutral bremsstrahlung. Thus, by comparing the measured absolute continuum radiation with the theoretical spectrum, T_e and n_e can be determined.

C. Determination of electron density and temperature from continuum radiation spectra

The continuum radiation requires the measurement of the absolute spectral irradiance (in [$\text{W m}^{-2} \text{nm}^{-1}$]). In this work, we only determined the time and spatially averaged absolute plasma emission through an absolute calibration of the spectrometer and detection system with a tungsten halogen lamp. The optical configuration for recording the global emission from the plasma is schematically shown in Fig. 2. The plasma reactor was placed at a distance of 0.5 m from a diaphragm with a diameter of 4.2 mm. The plasma emission through the diaphragm was focused into an optical fiber by a UV-visible plano-convex lens ($f = 7.5$ cm), which was then analyzed by a broadband spectrometer (Avantes 2048) with a spectral resolution of 0.6 nm. To achieve calibration, the calibrated tungsten halogen lamp (Oriel, Spectral Irradiance (250–2400 nm) 200 Watt QTH Lamp, Model No 63355) with known spectral irradiance at a distance of 500 mm was recorded by replacing the plasma source with the lamp and keeping all other optical components fixed and identical. At a distance of 500 mm, both the plasma and the light source can be considered as a point source and this simplifies the further analysis significantly. The absolute spectral irradiance, $I_P(\lambda)$ of the plasma is then given as follows

$$I_P(\lambda) = \frac{P(\lambda)}{L(\lambda)} I_L(\lambda) \quad (5)$$

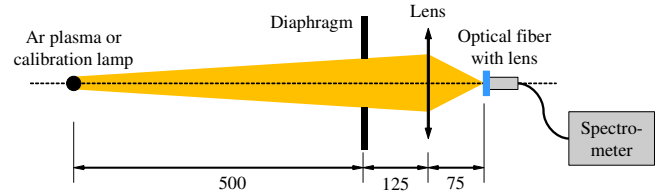


FIG. 2. Setup used for optical emission spectroscopy. The provided dimensions have mm units.

where $P(\lambda)$ and $L(\lambda)$ are the relative emission intensities from the plasma and the lamp, respectively, measured by the same optical detection system and $I_L(\lambda)$ is the spectral irradiance of the calibrated tungsten lamp at the same distance of 0.5 m. Now, the volume-averaged spectral emission coefficient or emissivity (in [$\text{W m}^{-3} \text{nm}^{-1}$]) of the Ar plasma can be obtained from the calibrated spectral irradiance, $I_P(\lambda)$ by^{41,42}

$$\langle j(\lambda) \rangle_V = I_P(\lambda) \frac{d^2}{V_P} \quad (6)$$

where d is the distance between the light source and the diaphragm (0.5 m) and V_P is the plasma volume. The calculated emissivity ϵ_{ea} from Eq. 4 is fitted to the measured spectral irradiance $\langle j(\lambda) \rangle_V$ to obtain a spatially averaged T_e and n_e . This fitting is performed in the range of $350 \text{ nm} \leq \lambda \leq 900 \text{ nm}$ since the spectral sensitivity of the calibrated halogen lamp drops significantly below 350 nm and the sensitivity of the spectrometer reduces significantly above 900 nm.

D. Electrical model

An independent determination of n_e is obtained by the analysis of an equivalent electrical circuit for a homogeneous RF plasma as reported in^{30,43}. This method is based on a simplified homogeneous RF discharge model without considering

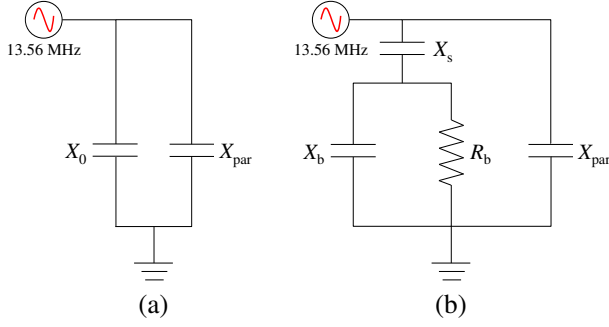


FIG. 3. Equivalent electrical circuit used for the calculations of the sheath width and the electron density with (a) plasma off, and (b) plasma on.

sheath effects (stochastic and ion heating),^{44,45} while isolating the influence of the bulk plasma and the sheaths. The assumptions used in this model are only valid for discharges operating in the α -mode, which is valid for the Ar plasma investigated in this study (see also further). This electrical model allows the determination of the electrical characteristics of the bulk plasma and the sheath, such as the plasma impedance, resistance and reactance. Fig. 3 shows the equivalent electrical circuit for the RF plasma under operation. For a detailed analysis of the equivalent electrical circuit, the reader is referred to⁴³. Briefly, the components of the equivalent electrical circuit, such as the sheath reactance (X_s), the bulk plasma reactance (X_b) and the bulk plasma resistance (R_b) can be obtained by solving the following equations⁴³

$$X_s = X_p + \frac{R_p^2}{X_p - X_0}, \quad (7)$$

$$X_b = X_0 - X_s, \text{ and} \quad (8)$$

$$R_b = R_p \left[1 + \frac{R_p^2}{(X_p - X_0)^2} \right], \quad (9)$$

where $X_0 = (\omega C_0)^{-1}$ is the reactance of the discharge gap without plasma with capacitance C_0 , and $R_p (= \frac{V}{I} \cos(\Delta\phi))$ and $X_p (= \frac{V}{I} \sin(\Delta\phi))$ are the real and imaginary parts of the plasma impedance, respectively. When the plasma is not ignited yet, the impedance should correspond to a purely capacitive reactance (Fig. 3a), with $C_0 = 0.8$ pF, however, the measured plasma-off impedance corresponds to a value of $C = (\omega X_p)^{-1} = 14.6$ pF. This huge deviation is caused by the additional stray or parasitic capacitances in the system, and are clubbed together as X_{par} by adding an additional parasitic capacitance, C_{par} parallel to the RF glow discharge in Fig. 3b, where $C_{\text{par}} = C - C_0 = 13.8 \pm 0.1$ pF. Considering C_{par} in the equivalent circuit, the current through the plasma

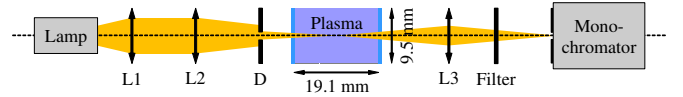


FIG. 4. Setup used for broadband absorption spectroscopy.

circuit was recalculated from the measured current. The time-averaged electron density can then be estimated from R_b using impedance measurement and a homogeneous plasma model⁴⁵

$$n_e = \frac{l - 2s_0}{AR_b} \frac{v_m m_e}{e^2}, \quad (10)$$

where l is the inter-electrode spacing (2 mm in this case), s_0 the time-averaged sheath width and A the cross-sectional area of the electrode. The rates of electron-neutral momentum transfer (v_m) for argon and helium at atmospheric pressure are $4.03 \times 10^{12} \text{ s}^{-1}$ and $1.52 \times 10^{12} \text{ s}^{-1}$, respectively.⁴⁶ Using the measured sheath capacitance X_s , the sheath width can be estimated as follows.^{30,44}

$$s_0 = \omega \epsilon_0 A X_s / 2, \quad (11)$$

where $\omega = 2\pi f$ is the plasma excitation frequency. The uncertainties in the time-averaged sheath width and the electron density are estimated by propagating the measurement uncertainties in C_{par} and $\Delta\phi_p$ through the equations of the equivalent electrical model.

E. Broadband absorption spectroscopy

The absolute densities of Ar atoms in metastable and resonant states across the plasma gap were determined by employing broadband absorption spectroscopy. The optical configuration for the spectrally resolved measurements is similar as used in³¹ and is shown in Fig. 4.

A laser-stabilized broadband lamp (Energetiq EQ-99 LDLS) was used as the light source. The light produced by the lamp was focused into the plasma reactor via lenses L1 ($f = 20$ cm) and L2 ($f = 10$ cm) through a diaphragm D with a diameter of 1 mm. After passing the reactor, the light was immediately focused onto the entrance slit of a 1 m high-resolution Czerny-Turner scanning monochromator (ARC AM-510), equipped with an 1800 g mm^{-1} grating blazed at 500 nm, via a plano-convex lens L3 ($f = 5$ cm). The width of the entrance slit was fixed at $10 \mu\text{m}$ and was located 5 cm from the lens L3. A neutral density filter was used in all the experimental conditions to avoid the saturation of the detector by the lamp. The spectrometer was backed by a $26 \mu\text{m}$ pitch charged-coupled device (CCD) camera (Andor iDUS 420). The spectral resolution of the optical system (monochromator + CCD), as deduced from the width of the atomic line of mercury in a low pressure Hg-Ar lamp, is 29 pm FWHM at 365 nm monitored in the 1st order of diffraction.

To obtain spatially resolved measurements, the plasma reactor was moved in steps of $50 \mu\text{m}$ along the plasma gap, on a translational stage. The spatial resolution was $40 \mu\text{m}$. For the determination of the spatial resolution within the plasma gap, the readers are referred to the procedure described in³¹.

F. Gas temperature

Due to the presence of a small concentration of water impurities in Ar and He + 17% Ar plasmas, we were able to record high resolution rotational spectra of OH(A-X)(0-0). In this case, a bandpass filter (240–420 nm), instead of a neutral density filter, was used. The experimentally measured emission spectra of OH(A-X) in different gas conditions were fitted with synthetic spectra obtained by following the modeling procedure described in⁴⁷ to determine the gas temperature. The reported uncertainties were derived from the 95% confidence interval using the least-square fitting procedure. An example of a recorded OH(A-X) emission spectrum along with the simulated best fit is shown in Fig. 5 for the He + 17% Ar plasma. The gas temperatures obtained from the rotational temperature of OH(A-X) are 365 K and 335 K for pure Ar and He + 17% Ar plasmas, respectively.

G. Absolute densities of atoms in resonant and metastable states

The different excited states and corresponding transitions investigated in this study are compiled in Table II. Density of Ar metastable atoms in $1s_3$ and $1s_5$ states, according to Paschen notation (or $4s'[1/2]_0$ and $4s[3/2]_2$ in Racah notation), are measured from absorption on 763.51 and 794.82 nm transitions, respectively. Density of atoms in resonance states $1s_2$ and $1s_4$ (or $4s'[1/2]_1$ and $4s[3/2]_1$), are measured by means of 750.39 and 751.47 nm lines, respectively. $1s_2$ and $1s_4$ states being optically connected to the ground state of Ar, these later lines are strongly broadened by resonance interaction (resonance broadening).

The detailed procedure for obtaining the absorption spectrum using broadband absorption spectroscopy is reported in^{31,48–50}. In brief, the experimental fractional absorption $A(\lambda)$ can be calculated as follows:⁴⁹

$$A(\lambda) = 1 - \frac{L_P(\lambda) - P(\lambda)}{L_0(\lambda) - B(\lambda)}, \quad (12)$$

where $P(\lambda)$ and $L_0(\lambda)$ are the emission spectra of the plasma and the lamp, respectively; $L_P(\lambda)$ is the emission spectrum of the plasma with the transmitted light of the lamp; and $B(\lambda)$ is the background spectrum with both plasma and lamp off. As an example, these emission spectra were recorded for $1s_2$, $1s_3$, $1s_4$ and $1s_5$ states in He + 17% Ar at the sheath edge, $250 \mu\text{m}$ from the powered electrode, and the corresponding fractional absorption spectra obtained using Eq. 12 are shown in Fig. 6. The absorption spectra for these states contained oscillations as reported in³¹, the amplitude of which were significantly

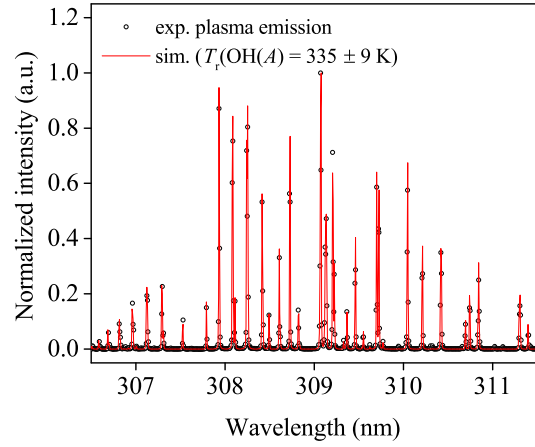


FIG. 5. Gas temperature determination from an experimentally recorded emission spectrum of OH(A-X) and the simulated best fit for He + 17% Ar plasma operating at 12.4 W and measured at a distance of $600 \mu\text{m}$ from the powered electrode surface.

attenuated by using FFT band block filters at frequency ranges of 0.18–0.2 per pixel and 0.086–0.095 per pixel. This induced an average difference of $\sim 10\%$ in the magnitude of the peak fractional absorption without affecting the total wavelength integrated area under the absorption line profile significantly.

The absolute path-averaged density, n , of the absorbing species can be determined by calculating the wavelength integrated area W under the fractional absorption curve for each of the above cited argon lines and using the Beer-Lambert law as follows:⁴⁹

$$W = \int A(\lambda) d\lambda = \int (1 - \exp(-\sigma(\lambda, T) \cdot n \cdot l)) d\lambda, \quad (13)$$

where T is the neutral gas temperature, σ the wavelength and temperature dependent absorption cross-section, and l the beam path length through the plasma (19.1 mm). As previously reported in⁴⁹, W is independent of the instrumental spectral resolution, and thus, can be experimentally determined by fitting the absorption profile for each line with a Voigt function as shown in Fig. 6. In Eq. 13, the absorption cross-section, σ (m^2), is given by

$$\sigma(\lambda, T) = \lambda_0^2 \frac{e^2}{4\epsilon_0 m_e c^2} f_{lu} \varphi(\lambda), \quad (14)$$

where λ_0 , e , ϵ_0 , m_e , c , f_{lu} and $\varphi(\lambda)$ are the peak wavelength of the observed transition (m), the elementary charge (C), the permittivity of the free space (F m^{-1}), the electron mass (kg), the speed of light in vacuum (m s^{-1}), the dimensionless oscillator strength of the line and the area-normalized spectral shape of the absorption line profile, respectively.⁴⁹ In high pressure plasmas with a low ionization degree as in the glow discharges studied, collisional broadening due to neutral collisions is the dominant effect, while natural broadening is negligible. Assuming a Maxwellian velocity distribution, $\varphi(\lambda)$

TABLE II. Different transitions of Ar and their characteristics.⁵¹

Observed wavelength (nm)	Resonant wavelength (nm)	Lower level	Upper level	Paschen notation	E_l (cm ⁻¹)	E_u (cm ⁻¹)	Oscillator strength
750.39	104.82	4s'[1/2] ₁	4p'[1/2] ₀	1s ₂	95400	108723	0.125 ^a , 0.2629 ^b
751.47	106.67	4s[3/2] ₁	4p[1/2] ₀	1s ₄	93751	107054	0.114 ^a , 0.0675 ^b
763.51		4s[3/2] ₂	4p[3/2] ₂	1s ₅	93144	106238	0.214
794.82		4s'[1/2] ₀	4p'[3/2] ₁	1s ₃	94554	107132	0.53

^a Oscillator strength of the observed transition.

^b Oscillator strength of the resonant transition.

can be regarded as a normalized Voigt function, for which the Gaussian component is due to Doppler broadening. The corresponding Doppler-broadened full width at half maximum (FWHM) is given by

$$\Delta\lambda_D(T) = \lambda_0 \times 7.16 \times 10^{-7} \times \sqrt{\frac{T}{M}}, \quad (15)$$

where M is atomic mass of the collider. The Lorentzian component arises because of collisions between the excited Ar atom and a ground state Ar atom. For lines ending in metastable states, which are not optically connected to the ground state, broadening is mainly by van der Waals interactions, while for the lines ending in the resonant states, additionally, resonance broadening needs to be considered. The analysis of both type of line profiles is discussed below.

The FWHM of the van der Waals broadening, which arises due to the dipole interaction of an excited Ar atom with the induced dipole in the ground state Ar (or He) atom, can be expressed as⁵²

$$\Delta\lambda_{\text{vdW}} [\text{nm}] = 3.0 \times 10^{-15} \lambda^2 (\Delta C_6)^{2/5} \left(\frac{T}{\mu_P}\right)^{3/10} N_P, \quad (16)$$

where λ is the wavelength of the observed transition (nm), ΔC_6 the Leonnard-Jones potential interaction constant, and μ_P the radiator-perturber reduced mass. For He-Ar and Ar-Ar interactions, the values of μ_P are 3.638 amu and 19.97 amu, respectively. N_P is the ground-state perturber density (cm⁻³). The value of ΔC_6 can be estimated from the following equation

$$\Delta C_6 = 9.8 \times 10^{-10} \alpha_P (\langle R_u^2 \rangle - \langle R_l^2 \rangle), \quad (17)$$

where α_P is the dipole polarizability of the perturber atoms (cm³) in their ground states and has values of 2.01×10^{-25} cm³ for He and 1.654×10^{-24} cm³ for Ar.⁵² $\langle R_i^2 \rangle$ is the mean square radius of the radiator atom in the upper and lower states of the observed transition of the perturbed atom (expressed in units of Bohr radius a_0). $\langle R_i^2 \rangle$ can be determined from Unsold's hydrogenic approximation as⁵³

$$\langle R_i^2 \rangle = \frac{1}{2} n_i^2 [5n_i^2 + 1 - 3l_i(l_i + 1)], \quad (18)$$

where l_i is the active electron orbital quantum number (0 for s and 1 for p) and n_i^2 is the effective principal quantum number of the state, given by

$$n_i^2 = \frac{E_{\text{ion}}^H}{E_{\text{ion}}^{\text{Ar}} - E_i}, \quad (19)$$

where E_{ion}^H is the ionization potential of the hydrogen atom or Rydberg constant, $E_{\text{ion}}^{\text{Ar}}$ the ionization potential of the radiator atom (Ar in this case) and E_i the energy of the considered state of the perturbed atom to which the observed transition belongs. Thus, for different concentrations of Ar in He-Ar plasma, $\Delta\lambda_{\text{vdW}}$ could be calculated with He and Ar as the perturber atoms. The total width of the vdW broadening is the sum of the individual width perturbed by He and Ar.

For resonance broadening, the FWHM (in nm) can be calculated as⁵²

$$\begin{aligned} \Delta\lambda_R &= 8.6 \times 10^{-28} \left(\frac{g_0}{g_1}\right)^{1/2} \lambda^2 \lambda_R f_{\text{lu}} N_{\text{Ar}} \\ &= \chi_{\text{Ar}} R_{\text{Ar}} \left(\frac{300}{T}\right) p, \end{aligned} \quad (20)$$

where λ and λ_R are the wavelengths of the observed and the resonance lines in nm, respectively, f_{lu} is the oscillator strength of the resonance line starting from the lower state of the transition (given in Table II), $g_1 = 3$ and $g_0 = 1$, the statistical weights of the lower level of the transition and of the ground state, respectively. N_{Ar} , χ_{Ar} , R_{Ar} and p are the argon ground state number density (cm⁻³), the fraction of Ar in the gas mixture, a constant for resonance broadening of Ar, and the pressure in bar, respectively.

The Stark broadening for the investigated experimental conditions is negligible due to the low electron density in such RF discharges.

The vdW broadening calculations are carried out only for lines ending in the metastable states as lower level (1s₃ and 1s₅). Since the resonance broadening dominates for 1s₂ and 1s₄ states, the vdW broadening has been neglected for these lines. The perturbation due to He and Ar are considered separately in determining the vdW broadening with Eq. 16,

$$\Delta\lambda_{\text{vdW}} [\text{nm}] = \chi_{\text{He}} K_{\text{He}} \left(\frac{300}{T}\right)^{0.7} + \chi_{\text{Ar}} K_{\text{Ar}} \left(\frac{300}{T}\right)^{0.7}. \quad (21)$$

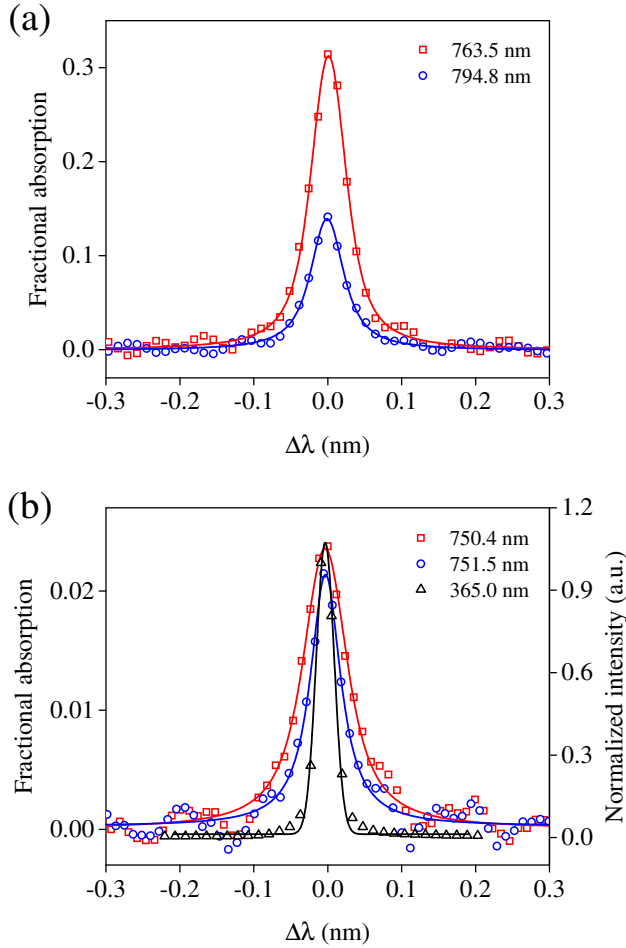


FIG. 6. Absorption profiles of atoms in (a) metastable states (763.5 and 794.8 nm), and (b) resonant states (750.4 and 751.5 nm) of Ar corresponding to He + 17% Ar plasma. The profiles are recorded at the sheath edge, 250 μm from the powered electrode. As a comparison, the slit function of the monochromator as determined by the normalized intensity of Hg I line recorded at 365 nm is also shown in (b).

χ_{He} is the fraction of He and $\chi_{\text{He}} + \chi_{\text{Ar}} = 1$. K_{He} and K_{Ar} are constants for vdW broadening. Table III compiles the values of these constants. However, as one can see from absorption profiles presented in Fig. 6, their noise level is too high to permit a correct determination of the broadening parameters. We, thus, have used the line profiles of the emission spectra $P(\lambda)$ recorded for the broadband absorption spectroscopy measurements, which have much higher signal/noise ratios (see Fig. 11 in Section III B), for the determination of the pressure broadening constants of the lines reported in Table III.

The convolution of the Gaussian FWHM ($\Delta\lambda_{\text{D}}$) and the Lorentzian FWHM ($\Delta\lambda_{\text{L}}$) profiles provides the Voigt function to be used as the normalized $\varphi(\lambda)$ in Eq. 14. For a fractional absorption of only a few %, W can be directly deduced by a linear approximation of the term $(1 - \exp(-\sigma(\lambda, T) \cdot n \cdot l))$ in Eq. 13 to $\sigma(\lambda, T) \cdot n \cdot l$, and thus the density, n can be directly determined using equations Eqs. 13–20. However, for

TABLE III. Measured van der Waals and resonance broadening constants of used Ar lines scaled for atmospheric pressure and 300 K in pure Ar and He.

State	K_{He} (nm)	K_{Ar} (nm)	R_{Ar} (nm)
$1s_3$	0.023	0.032	–
$1s_5$	0.020	0.028	–
$1s_2$	–	–	0.189
$1s_4$	–	–	0.050

strongly absorbing lines, due to the non-linearity of W as a function of n , there is no analytical expression to relate these two parameters. Therefore, a simulation was performed to deduce W for different values of n .^{31,49} The experimentally measured values of W were compared with those of simulated W to determine the absolute time-averaged and line-of-sight integrated densities of atoms in $1s_2$, $1s_3$, $1s_4$ and $1s_5$ states of Ar. The reported uncertainties on the estimated densities were determined from twice the standard deviation based on the uncertainties in the fitting of the Voigt profile to the absorption line profile to determine W and the asymmetry in the spatially distributed density profile. The uncertainties due to the estimated error in the gas temperature determination were negligible. Moreover, there exists uncertainty in the spatial variation of the experimental data. For instance, spatial variations of $\sim 20\%$ were observed in the density profiles of the $1s_3$ and $1s_5$ metastable states, which could be increased to 45% close to the detection limit, in pure Ar discharge.

H. Resonance radiation transport modeled by Monte Carlo simulation

To explain the measured profile of atoms in resonance states in the discharge, we implemented a resonance radiation transport model. We considered the argon lines $3s^23p^6 - 3s^23p^5(^2P_{1/2}^0)4s$ (104.8 nm) and $3s^23p^6 - 3s^23p^5(^2P_{3/2}^0)4s$ (106.7 nm) in an optically thick slab corresponding to the plasma volume within 2 mm gap between the electrodes. The density of photo-excited atoms has been estimated using a kinetic Monte Carlo method; details can be found in^{54–56}. The inter-electrode gap is divided into 100 slabs of 20 μm thickness each, which form the grid points for the Monte Carlo simulation. The 20 μm thickness of the slabs enables to resolve the 50 μm spatial resolution of the experiment.³¹ The two slabs at a distance of 0.4 mm from the walls corresponding to the locations where the maximum densities of atoms in the resonant states were measured (see further) are taken to be the source of the initial photons for this simulation. In this method, random walks for photons are generated numerically and they serve in the evaluation of the number of absorption processes that occur at a given location z in each slab. At each walk, a photon “birth” is first performed through random generation of the position \mathbf{r} , the wavelength λ , and the direction $\mathbf{n} = \mathbf{k}/|\mathbf{k}|$. The angles θ and ϕ relative to the direction \mathbf{n} (expressed using the spherical coordinates) are gener-

ated using a uniform distribution for $\cos \theta \equiv \mu$ and for ϕ . The wavelength λ is generated assuming a Lorentzian distribution, $\phi(\lambda)$, accounting for collisional broadening. Once z , θ , ϕ and λ have been generated, the path length s covered by the photon before its absorption by an Ar atom is generated using an exponential distribution, of parameter $a(\lambda)$, the mean free path of the photon, defined as $a(\lambda) = 1/([Ar] \cdot \sigma(\lambda))$, where $[Ar]$ is the density of argon atoms and $\sigma(\lambda)$ is the absorption cross section, given in Eq. 14, but with λ_0 and f relative to the resonance transition. Note that the photon path length s is wavelength dependent. The absorption occurs at the coordinate $\mathbf{r}' = \mathbf{r} + \mathbf{n}s$. During the lifetime of the newly excited atom, the proportion of emission of a new photon is estimated using the branching ratio $A_{ul}/(A_{ul} + C_{ul})$ where A_{ul} is the Einstein coefficient for spontaneous emission and C_{ul} is the collisional de-excitation frequency. A uniform random variable in the $[0,1]$ interval, u , is generated and provides the process that occurs (photon emission if $u < A_{ul}/(A_{ul} + C_{ul})$; quenching otherwise) at the location \mathbf{r}' . In the case where a photon emission process occurs, new values are generated for the direction \mathbf{n} , the wavelength λ , and the path length s , according to the procedure indicated above. In the quenching case, the random walk ends. The simulation ends once a given number of random walks has been performed. The calculation yields the photo-excitation rate W_{lu} (s^{-1}) at the z location within the 100 grid points. The total number of initially generated photon + photon absorption occurring at each grid point is evaluated using a counter. This quantity is representative of the density of atoms in the resonance state. About 10^6 initially generated photons, followed by random walks, was necessary in order to have a reasonable (> 100) signal/noise ratio on calculated densities.

III. RESULTS AND DISCUSSIONS

A. Determination of T_e and n_e

Fig. 1(b)–(d) present emission images of plasmas in Ar, He and He + 17% Ar, respectively. The intense bright “white” emission in the bulk of the pure Ar discharge shown in Fig. 1(b) suggests the presence of continuum radiation in the visible wavelengths. The measured time and spatially averaged absolute emission spectra of the RF-driven capacitive discharges in Ar and He and the fitted theoretical spectra are shown in Fig. 7. This measured emission spectrum is fitted with the calculated emissivity of the neutral bremsstrahlung radiation (ϵ_{ea}) following the procedure described in Section II B. The fit was performed by matching the lowest intensity features of the spectra in their high wavelength sides. For argon, the fit suggests the presence in the 450–650 nm range of emission having another origin.

The neutral Bremsstrahlung ϵ_{ea} is calculated by using both Maxwellian and non-Maxwellian EEDFs via the Boltzmann solver Bolsig+³⁸ (cross-section obtained from^{40,57}) as the EEDF deviates significantly from a Maxwell-Boltzmann distribution.^{58,59} The obtained electron properties (T_e and n_e) are shown in Table IV. For the calculation of the non-

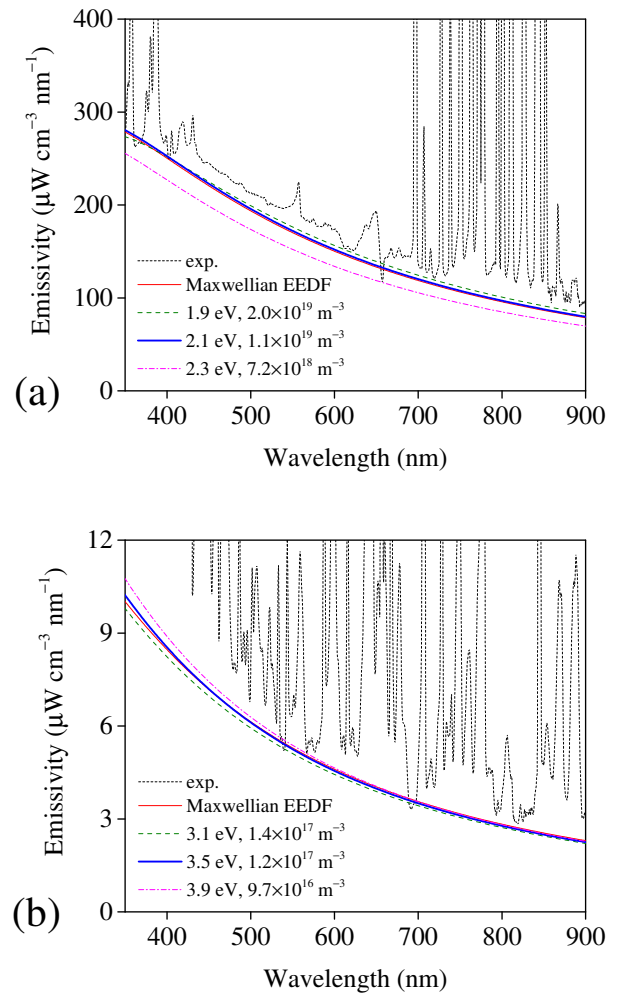


FIG. 7. The measured absolute intensity of RF plasma emission in (a) Ar at a discharge power of 13.5 W and (b) He at a discharge power of 14.0 W, and gas flow rate of 1 slm fitted with the calculated emissivities of the e-a bremsstrahlung continuum radiation using both Maxwellian and non-Maxwellian EEDFs. The obtained values for Ar and He plasmas are reported in Table IV.

Maxwellian EEDF, an ionization degree of 10^{-7} was used. The uncertainty in the absolute calibration due to day-to-day variation in the intensity of plasma and halogen lamp emissions was $\sim 12\%$, while the random variation in the absolute intensity was $\sim 14\%$ for helium and $\sim 12\%$ for argon. The random uncertainty due to the experimental variation between different measurements were negligible as compared to the aforementioned uncertainties. The final uncertainty in the electron density was estimated by using the root mean square error. While the relative calibration is more accurate than the absolute calibration, the uncertainty in n_e also leads to additional uncertainty in T_e . The fit resulted in an effective T_e of 2.1 ± 0.3 eV for argon and 3.5 ± 0.4 eV for helium. The fit also yielded an n_e of $(1.1 \pm 0.7) \times 10^{19} \text{ m}^{-3}$ for argon and $(1.2 \pm 0.2) \times 10^{17} \text{ m}^{-3}$ for helium. However, a Maxwellian distribution led to a significantly lower T_e for both Ar and He,

with an n_e , which is ~ 5 times higher to obtain the same profile, particularly for Ar (Table IV). This suggests that it is important to consider non-Maxwellian effects in the EEDF to obtain accurate T_e and n_e from neutral bremsstrahlung measurements.

An alternative and independent approach to measure the electron density is using plasma impedance measurements, as described in Section II D. The voltage and current waveforms for Ar plasma operating at a discharge power of 13.5 W with an applied peak-to-peak voltage of 853 V and a current of 1.3 A are shown in Fig. 8. The sheath width calculated for these parameters from the equivalent electrical model described in Section II D is $180 \mu\text{m}$. Additionally, the sheath width was obtained from optical images of the discharge at the same operating conditions. The digital images were converted to spatially-distributed intensity profiles by binning the pixels in the vertical direction (not shown here) and then normalized with respect to the maximum intensity for better visualization. These normalized total intensity profiles for discharge in Ar and He are shown in Fig. 9. The apparent peaks at positions 0 (grounded electrode) and 2 mm (powered electrode) are most likely due to the grazing-angle reflections of the plasma emission by electrodes. Finally, the sheath width was determined by the difference in the number of pixels when the intensity drops to 61% of the intensity at the sheath edge.^{30,45} The sheath edge is marked by a horizontal gray dashed line in Fig. 9. This yielded a sheath width of $170 \mu\text{m}$ in pure argon discharge, which is very similar to that determined from the electrical model within the accuracy of the experiment. Using Eq. 10 and Eq. 11, the n_e is calculated to be $1.3 \times 10^{18} \text{ m}^{-3}$, which is an order of magnitude lower than the n_e determined by neutral Bremsstrahlung assuming a non-Maxwellian distribution. The same procedure was followed to obtain $s_0 = 380 \mu\text{m}$ and $n_e = 1.8 \times 10^{17} \text{ m}^{-3}$ for He. The electron density is of the same order of magnitude as obtained from the neutral Bremsstrahlung. However, the sheath width obtained from the optical images was found to be $160 \mu\text{m}$, which is much smaller than that obtained from the electrical model. A summary of the sheath widths and electron densities as calculated from the equivalent electrical model for Ar and He RF glow discharges as functions of discharge power are shown in Fig. 10. Similar trends and values are obtained for the RF COST reference microplasma jet operating in the abnormal or α -mode with an inter-electrode gap distance of 1 mm.⁶⁰

An independent estimate of T_e can be obtained from the power balance. Assuming momentum transfer from electrons to neutrals by elastic collisions as the dominant loss mechanism, the input electrical power density, $P/V [\text{W m}^{-3}]$ can be written as follows⁴⁴

$$\frac{P}{V} = n_e n_a k_{el}(T_e) \frac{3m_e}{m_{Ar}} k_B (T_e - T), \quad (22)$$

where k_{el} is the rate constant for elastic electron scattering on Ar calculated by Bolsig+.⁶¹ The ionization and excitation rate constants are neglected in Eq. 22 as these are several orders of magnitude lower than k_{el} in the investigated operating conditions. Using Eq. 22, at $P/V = 37.2 \text{ W cm}^{-3}$ assuming

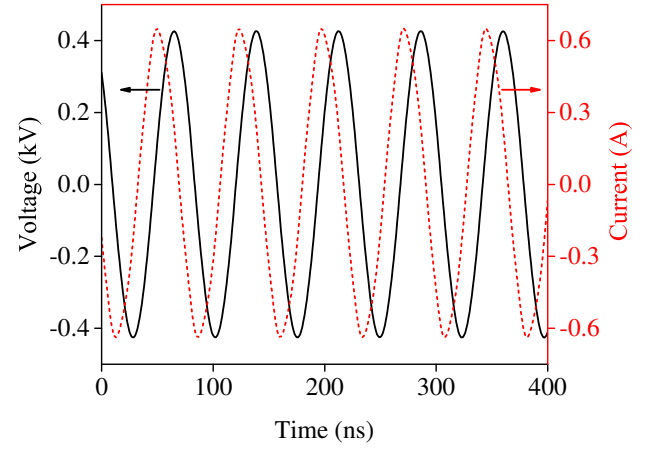


FIG. 8. Voltage and current waveforms of the Ar RF glow discharge.

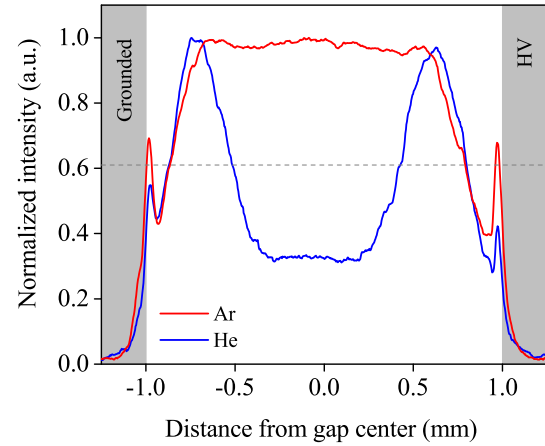


FIG. 9. Normalized total emission intensity profiles of Ar and He RF glow discharges at discharge powers of 13.5 W and 14.0 W, respectively. The shaded regions represent the location of the grounded and the high-voltage (HV) electrodes.

V is equal to the entire plasma volume, T_e was evaluated at the same n_e as obtained from continuum emission fitting approach and found to be 1.2 eV for Ar. Similarly, assuming a T_e of 2.1 eV, a mean electron density of $2.2 \times 10^{18} \text{ m}^{-3}$ was obtained. The same approach was applied to the He case and the results are shown in Table IV. The obtained electron temperature from the power balance in Ar (1.2 eV) is much lower than that obtained from the continuum radiation approach. While the power approach is an approximation, a possible explanation for the higher T_e obtained from the continuum radiation measurement is the contribution of a higher T_e in the near sheath region due to the non-local electron kinetics effects. Indeed, particularly in Ar, the length scale of electron energy relaxation at atmospheric pressure as given by⁶²

$$\lambda_e = \frac{\lambda_e}{\sqrt{\delta}} \quad (23)$$

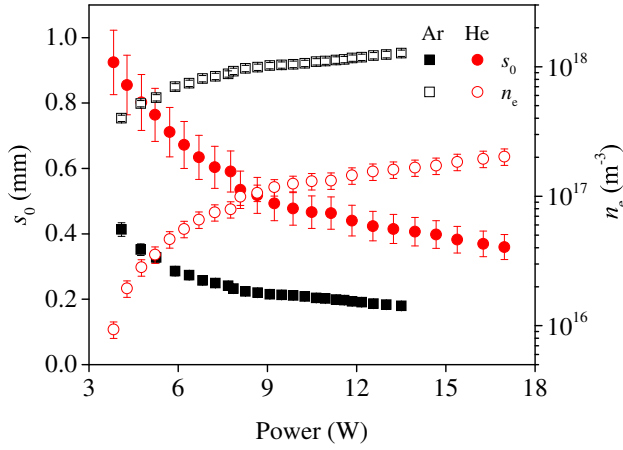


FIG. 10. Time-averaged sheath width and electron density as a function of the discharge power for Ar and He RF glow discharges obtained using Eq. 10 and Eq. 11.

is large ($\sim 240 \mu\text{m}$). In Eq. 23, λ_e is the mean free path of electron in Ar and $\delta = 2m_e/m_{\text{Ar}}$. Hence, a significant part of the inter-electrode gap can contain electrons with a much higher energy than estimated from a bulk local field approximation analysis. In addition, the power dissipated in the sheath is unknown and not accounted for, which leads to additional uncertainties.

For a similar geometry with 2 mm inter-electrode gap, a driving frequency of 13.56 MHz and similar power density in Ar, the modeling results reported an n_e of $8 \times 10^{17} \text{ m}^{-3}$ in the bulk and a T_e of $\sim 2.5 \text{ eV}$.⁶³ This model accounted for the deviations from Maxwellian distribution by calculating the EEDF from Bolsig+ and also included stepwise ionization as one of the prominent electron production mechanisms in the plasma. Using similar model, but with a different geometry, an n_e of $7 \times 10^{17} \text{ m}^{-3}$ was reported, while the T_e varied from 2.1 eV to 2.9 eV within one RF discharge cycle.⁶⁴ Although the calculated n_e in these models is lower than that determined in the current study, the space-averaged T_e is similar. An experimental study on Ar and He RF discharges at atmospheric pressure used the current density and a steady-state power balance to determine n_e and T_e .⁶⁵ Although the reported T_e values for both Ar and He plasmas are lower (1.1 eV) than that determined in the current study, n_e value for Ar plasma ($(2.4 \pm 0.5) \times 10^{18} \text{ m}^{-3}$) is of the same order of magnitude as estimated in this study within the experimental error, while it is almost an order of magnitude larger in He ($(9.3 \pm 1.8) \times 10^{17} \text{ m}^{-3}$). A one-dimensional fluid model applied to an Ar RF discharge operating at atmospheric pressure using a similar electrical model analysis as⁶⁵ reported an n_e of $\sim 2 \times 10^{18} \text{ m}^{-3}$,⁶⁶ which is 5.5 times smaller than the value estimated in this study. A self-consistent computational study of a He RF discharge reported an n_e of $3.6 \times 10^{17} \text{ m}^{-3}$, only thrice the value determined in the current study.⁶⁷

Thus, from these reported results, it is evident that different methods (continuum radiation, electrical model and power balance) yield different values of n_e and T_e . While both elec-

TABLE IV. Comparison of electron properties (T_e and n_e) of RF-driven capacitive Ar and He glow discharges at atmospheric pressure with a discharge power of 13.5 W and 14.0 W, respectively obtained from the continuum radiation ϵ_{ea} fitting with the assumption of a Maxwellian EEDF and non-Maxwellian EEDF.

Method	Ar		He	
	T_e (eV)	n_e (m^{-3})	T_e (eV)	n_e (m^{-3})
Continuum radiation				
Maxwellian EEDF	1.1	5.3×10^{19}	2.5	2.0×10^{17}
Non-Maxwellian EEDF	2.1	1.1×10^{19}	3.5	1.2×10^{17}
Electrical model	–	1.3×10^{18}	–	1.8×10^{17}
Power balance	1.2	(1.1×10^{19})	3.1	(1.2×10^{17})

trical model and power balance methods have assumptions, and, in particular for He, which do not account for important impact of impurities leading to Penning ionization,^{68,69} the only uncertainty in the continuum radiation approach is mainly due to the fitting and absolute calibration of the continuum emission intensity. Thus, the continuum radiation approach is believed to be the most accurate.

In summary, the time and space-averaged T_e and n_e values determined from the continuum emission of the argon plasma are $2.1 \pm 0.3 \text{ eV}$ and $(1.1 \pm 0.7) \times 10^{19} \text{ m}^{-3}$, respectively, while for helium plasma, a T_e of $3.5 \pm 0.4 \text{ eV}$ and an n_e of $(1.2 \pm 0.2) \times 10^{17} \text{ m}^{-3}$ are determined.

B. Measured Ar line widths

The collisional broadenings, or the Lorentzian widths of Ar lines used in this study for the measurement of Ar(1s) atoms density in both metastable and resonant states, were determined from the plasma induced emission spectra, as shown in Fig. 11 for the 750 nm spectral region, recorded in pure argon plasma. The gas temperature, obtained from the rotational temperature of OH(A–X) emission (see Section II F), is 365 K in this plasma. Fitting the profiles of these lines with Voigt functions provides their Gaussian and Lorentzian widths. In the example of Fig. 11, the best fit of the 751.5 nm line is obtained with $w_G = 2.27 \pm 0.38$ pixels and $w_L = 4.17 \pm 0.26$ pixels, for the Gaussian and Lorentzian widths, respectively. Uncertainties are twice the standard deviations from the fit. With the 11.47 pm/pixel linear dispersion of the spectrometer, deduced from the numbers of pixels between the positions of 750.4 and 751.5 nm lines, the widths in pixel are converted to $\Delta\lambda_G = 26 \pm 4 \text{ pm}$ and $\Delta\lambda_L = 48 \pm 3 \text{ pm}$. Given that at 365 K the Doppler widths of the 750 nm lines are only about 1.6 pm, we can conclude that $\Delta\lambda_D$ can be neglected and $\Delta\lambda_G = 26 \pm 4 \text{ pm}$ corresponds to the instrumental width. This apparatus width is slightly smaller than the 29 pm deduced from the 365 nm Hg line width, as shown in Fig. 6(b). The difference is in accordance with the reduction of the linear dispersion of the spectrometer with increasing rotation angle of the grating, thus with the wavelength. Fixing the same instrumental

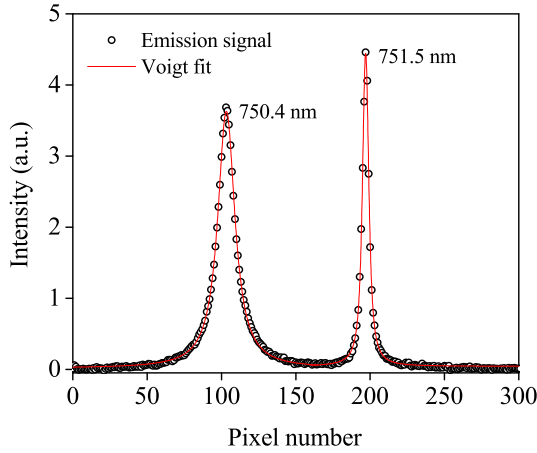


FIG. 11. Experimentally recorded emission spectra of Ar($1s$) lines in the resonant states fitted with a Voigt profile for pure Ar discharge operating at 13.5 W and measured 250 μm away from the electrode surface.

width $w_G = 2.27$ pixels for the fit of the 750.4 nm line, we obtain the Lorentzian width of the line $w_L = 13.5 \pm 0.2$ pixels, corresponding to $\Delta\lambda_L = 155 \pm 3$ pm. From the above deduced w_L values in pure Ar plasma at $T_g = 365$ K, the broadening coefficients at “standard conditions” of 1 atmosphere and 300 K would be 58 ± 4 and 189 ± 4 pm for 751.5 nm and 750.4 nm lines, respectively. Following the same procedure, the Lorentzian widths of the 763.5 nm and 794.8 nm lines have been deduced from the Voigt fits of their emission spectra (not shown) recorded in pure argon plasma. With fixed Gaussian width of $w_G = 2.27$ pixels, the deduced Lorentzian widths are 2.68 ± 0.08 and 2.77 ± 0.10 pixels for 794.8 and 763.5 nm lines, respectively. Taking into account the uncertainty on $w_G = 2.27 \pm 0.38$ pixels, the above values lead to $\Delta\lambda_L = 30.8 \pm 4.5$ and 31.7 ± 4.5 pm at 365 K for these lines. These values correspond to $\Delta\lambda_L = 35 \pm 5$ pm for the 794.8 nm line and $\Delta\lambda_L = 36 \pm 5$ pm for the 763.5 nm line at 1 atmosphere and 300 K. Our experimental values are compiled in Table V, as well as the theoretical broadening coefficients, deduced from Eq. 20 and Eq. 21, and those reported in the literature. The pressure range and the estimated temperatures, as reported by authors, are also included in this table and, for the sake of clarity, all reported broadening coefficients are converted to their “standard conditions” of 1 atmosphere and 300 K, by using the temperature dependence of $\Delta\lambda_L$, as indicated in Eq. 20 and Eq. 21. The reported uncertainty in column 2 accounts for the uncertainty deduced from the fit plus the 2.7% uncertainty in the determination of the gas temperature.

The measured broadening coefficient of 750.4 nm line is in perfect agreement with its theoretical value and very close to the mean value of coefficients reported in^{70,72} and⁷⁴. These later have been measured in atmospheric pressure thermal plasmas, in which the plasma is usually not spatially homogeneous and the determination of the correct gas temperature is a hard task and is further complicated by additional Stark broadening of the lines. Our experimental coefficient for the

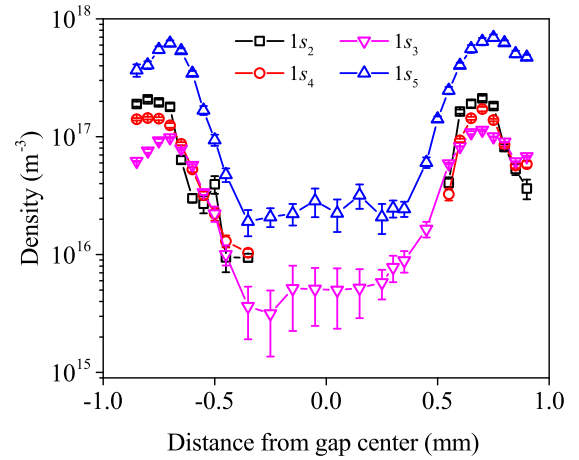


FIG. 12. Time-averaged spatially resolved absolute densities of atoms in $1s_2$, $1s_3$, $1s_4$ and $1s_5$ states of argon in pure Ar plasma at a discharge power of 13.5 W and total gas flow rate of 1 slm.

751.5 nm line being almost 20% larger compared to the theoretical one, can be justified by a contribution from the van der Waals broadening of the upper and lower states of the 751.5 nm line. In fact, the theoretical values reported in the 3rd column of Table V for 750.4 and 751.5 nm lines represent only the resonance broadening of the lower states of these transitions, $1s_2$ and $1s_4$ states, respectively. Values reported in⁷¹ and⁷² have been obtained from the emission line profiles in glow discharges, analyzed with a Fabry-Perot interferometer. At the low working pressures in these works, the Lorentzian width of the lines was comparable, or even smaller than the Doppler width, introducing large uncertainty on deduced $\Delta\lambda_L$. Reported uncertainties on the broadening coefficient of 751.5 nm line are $\pm 23\%$ in⁷¹ and $\pm 18\%$ in⁷². Our result for the van der Waals broadening of 794.8 nm line is in perfect agreement with the calculated and previously reported values. But for 763.5 nm lines, we have measured slightly larger value than the calculated one and those reported in the literature. Note that the uncertainties on these later broadening coefficients are large. However, considering that, with the estimated $n_e \leq 10^{19}$ m^{-3} (see Table IV) the Stark broadenings of the lines are negligibly small⁷⁵ and the high precision on measured gas temperature, we are reasonably confident on our measured $\Delta\lambda_L$ values reported in the 2nd column of Table V.

C. Spatial distribution of Ar atoms in metastable and resonant states

1. Ar RF glow discharge

The absolute densities of atoms in metastable ($1s_3$ & $1s_5$) and resonant ($1s_2$ & $1s_4$) states are determined following the detailed procedure described in Section II G. Fig. 12 shows the spatial distribution of the absolute densities of these atoms in the inter-electrode gap of pure argon discharge as a function of distance.

TABLE V. Pressure broadening coefficients by argon of the lines used for the determination of Ar($1s$) atoms density. For the sake of clarity all $\Delta\lambda_L$ values are for the “standard conditions” of 1 atmosphere at 300 K and previously reported widths are re-scaled for their temperature dependence by using Eq. 20 and Eq. 21.

Wavelength (nm)	$(\Delta\lambda_L)_{\text{exp}}$ (pm)	$(\Delta\lambda_L)_{\text{theory}}$ (pm) ^a	$(\Delta\lambda_L)_{\text{previous experiments}}$ (pm)						
			70	53	71	72	73	74	
Ref	This work								
P (bar) ^b	1	1	0.5–2	≤ 0.02	≤ 0.1	≤ 0.02	≤ 0.02	1–2.5	1–3
T_g (K) ^c	365	300	1130	300	360–500	300	300	2000	3900
750.4 ($1s_2$)	189 ± 9	188	213	–	–	–	208	–	165
751.5 ($1s_4$)	58 ± 6	49	59	–	–	41	48	75	57
763.5 ($1s_5$)	36 ± 6	28	–	30	–	–	–	32	22
794.8 ($1s_3$)	35 ± 6	32	31	–	–	–	–	30	20

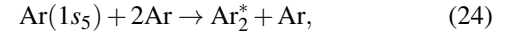
^a From Eq. 20 and Eq. 21

^b Gas pressure

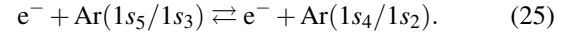
^c Estimated temperature

The density profiles in these states correlate well with the excitation zone in an RF-driven atmospheric pressure discharge operated in α -mode.^{67,76} A maximum density of atoms in metastable and resonant states in excess of 10^{17} m^{-3} are observed near the sheath edge region, 250–300 μm away from the electrodes, while the densities decline towards the electrodes and in the bulk plasma. The absolute densities of Ar atoms in $1s_3$ and $1s_5$ metastable states are more than an order of magnitude smaller in the bulk plasma than in the sheath region. A similar trend is observed for the absolute densities of Ar in $1s_2$ and $1s_4$ resonant states, with densities dropping below the detection limit in the bulk of the plasma. The density maxima near the sheath region are due to the elevated E/N in this region, leading to enhanced excitation and ionization rates in this region.³ The peak density of atoms in $1s_5$ state is the highest ($7 \times 10^{17} \text{ m}^{-3}$), while the lowest density at the same location is that of atoms in $1s_3$, the other metastable state ($9.7 \times 10^{16} \text{ m}^{-3}$). The major production mechanism of Ar atoms in the $1s$ states is electron-impact excitation from the ground state, directly or after radiative cascades from 2p states, following their excitation.²¹ Assuming a Maxwellian EEDF, with $T_e = 1.1 \text{ eV}$ and $n_e = 5.3 \times 10^{19} \text{ m}^{-3}$ obtained from the continuum emission measurement (see Table IV), the production rate could be as high as $6 \times 10^{25} \text{ m}^{-3}\text{s}^{-1}$ for the $1s_5$ state.^{18,77} However, as the ground-state excitation rate coefficients are highly sensitive to a variation of EEDF,¹⁸ a non-Maxwellian EEDF strongly impacts this reaction rate, and the production rate will be reduced by more than 3 orders of magnitude, $2.5 \times 10^{22} \text{ m}^{-3}\text{s}^{-1}$.³⁸ In this case, a non-Maxwellian EEDF increases the likelihood of other dominant reaction mechanisms for the $1s_5$ production. In an atmospheric pressure Ar glow discharge, Ar^+ ions produced by ionization are rapidly converted by 3-body reaction involving two Ar atoms, into Ar_2^+ dimer ions,⁶³ which rapidly recombine with electrons to produce Ar atoms in excited states; all these excited atoms ending finally in $1s$ states.

The dominant mechanism for the destruction of $1s_5$ and $1s_3$ metastable atoms is via the three-body collision with the ground-state argon atoms forming argon excimer:⁷⁸



and by the electron collision induced transfer to the $1s_4$ and $1s_2$ resonant states:^{2,21,28}



However, the reverse transfers of reaction 25 have comparable rate coefficients^{28,29} and instead of introducing a net loss of population in metastable states, the electron collision induced transfer reactions should be considered as partial population mixing mechanisms between the four $1s$ states. With the rate coefficient reported in⁷⁸: $k_{24} = 1.1 \times 10^{-44} \text{ m}^6 \cdot \text{s}^{-1}$, the 3-body quenching frequency of $1s_5$ metastable atoms in pure argon would be $4.5 \times 10^6 \text{ s}^{-1}$.

Besides volume quenching, the metastable species also diffuse across the gas volume and de-excite when impacting on the reactor walls. The diffusion timescale is given by

$$\tau_{\text{diff}} = \Lambda^2 / D_{\text{eff}} \quad (26)$$

where Λ , the characteristic length scale is given by $\Lambda = L/\pi$, with $L \approx 300 \mu\text{m}$ being the distance to the electrode of the maximum $1s_5$ metastable density and D_{eff} the binary diffusion coefficient, whose value is $1.0 \times 10^{-5} \text{ m}^2\text{s}^{-1}$ for Ar($1s_5$) in atmospheric pressure Ar at 365 K.⁷⁸ The diffusion time, estimated as 1 ms, is more than 3 orders of magnitude longer than the time for the collisional quenching of $1s_5$ state by 3-body reaction 24 (0.2 μs). Thus, the metastable atoms are primarily lost by collisional processes in the plasma volume. This would also mean that their recorded density profile corresponds exactly to the axial profile of their production rate.

For $1s_3$ metastable atoms, even with slightly different rate coefficients for their production,²¹ quenching,²⁵ and state mixing^{28,29} than for $1s_5$ atoms, their kinetics is similar to that of $1s_5$ atoms and except for the absolute values, their density profiles are almost identical.

Densities of atoms in resonant states ($1s_4$ and $1s_2$), shown in Fig. 12, are also similar to those of metastable atoms. The production mechanisms for these resonant states include also direct and cascaded electron-impact excitation from the ground-state and $e\text{-Ar}_2^+$ dissociative recombination. Electron-induced transfers between these states and metastable states ($1s_5$ and $1s_3$) cannot be considered as a net gain or loss mechanisms for the population of these states. Globally, the $1s_5$ state is receiving more than what is transferred from it to the other $1s$ states, the fact which, together with its largest statistical weight, explains the highest density of this state. However, the number of atoms transferred in one way and in the opposite way are comparable, within a factor of about 2. As an example, with rate coefficients reported in²⁹ and an electron density of $1 \times 10^{19} \text{ m}^{-3}$, the $1s_5 \rightarrow 1s_4$ transfer frequency would be $1.9 \times 10^6 \text{ s}^{-1}$ and $3.1 \times 10^6 \text{ s}^{-1}$ for the reverse transfer $1s_4 \rightarrow 1s_5$. These values are about 2-3 times smaller than the 3-body quenching frequencies of these states. We thus can conclude that, under our experimental conditions, e-impact transfers are not an important process for controlling the density of $1s$ states.

The radiative lifetimes, τ_{rad} of the $1s_2$ and $1s_4$ states are 1.88 and 7.58 ns,⁵¹ respectively. However, due to the resonance radiation trapping,^{79,80} the effective radiative decay time of population of these states rises to about 0.37 and 1.48 μs for $1s_2$ and $1s_4$ states, respectively, when the pure argon gas medium is approximated by two infinite parallel-plan limited slab of 2 mm thickness, an acceptable approximation to illustrate radiation trapping for the experimental conditions in our case. These global effective lifetimes, τ_{eff} are calculated using the Walsh model,⁸¹ which is the generalization of the Holstein theory.^{79,80} Atoms in resonance states are also quenched by 3-body collisions (similar to 24) and rate coefficients reported in⁷⁸ for $1s_2$ and $1s_4$ states are $k_{24}(1s_2) = 2.4 \times 10^{-45} \text{ m}^6 \text{ s}^{-1}$ and $k_{24}(1s_4) = 1.2 \times 10^{-44} \text{ m}^6 \text{ s}^{-1}$, respectively. In pure argon at 365 K, they lead to quenching frequencies ν_q of about $1.0 \times 10^6 \text{ s}^{-1}$ and $5.1 \times 10^6 \text{ s}^{-1}$ for $1s_2$ and $1s_4$ states, respectively. Comparing for each state the global radiative decay frequency, $1/\tau_{\text{eff}}$ and the 3-body loss frequency, one can conclude that the photon emission controls the decay of the global density of atoms in the $1s_2$ state but the 3-body collisions are dominant loss mechanism for atoms in the $1s_4$ state.

2. He + 17% Ar RF glow discharge

Fig. 13 shows the spatial distribution of density of atoms in the investigated excited states of argon in 17% Ar in He gas mixture. The density profiles are almost similar to those shown for the pure argon in Fig. 12 and correspond well with the emission profile of the plasma shown in Fig. 1d. Peak density of atoms in metastable ($1s_3$, $1s_5$) and resonant ($1s_2$, $1s_4$) states are measured near the sheath region, 400 μm away from the electrode surface. The maximum absolute density of slightly larger than 10^{18} m^{-3} is observed for the $1s_5$ state. Compared to the pure Ar discharge, the peak metastable $1s_3$ and $1s_5$ densities are about two times larger but those of reso-

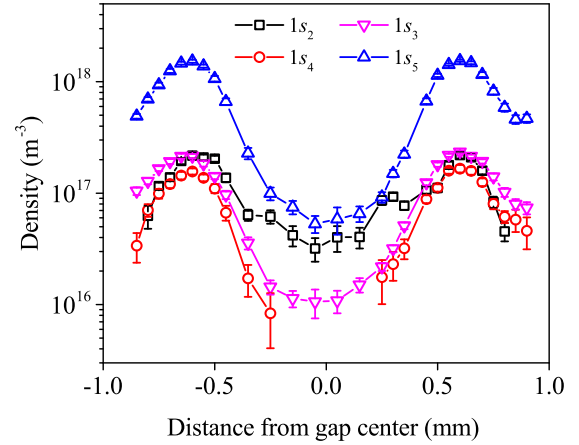
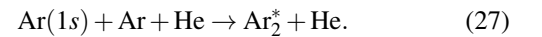


FIG. 13. Time-averaged spatially resolved absolute densities of atoms in $1s_2$, $1s_3$, $1s_4$ and $1s_5$ states of argon in He + 17% Ar plasma at a discharge power of 12.4 W and total gas flow rate of 1 slm.

nance states $1s_2$ and $1s_4$ are almost similar and about one order of magnitude lower than that of the $1s_5$ state. The densities decay when going away from the sheath region and at the central part of the plasma, drop below the detection limit for $1s_4$ resonant state. The peaks seem to be broader than in pure Ar and also slightly farther from electrodes (Fig. 12), which suggests a wider excitation zone. Helium being the main constituent of this plasma, an order of magnitude lowering of the electron density and an enhancement of T_e is expected, relative to the pure argon plasma (see Fig. 10 and Table IV). The main consequences in the kinetics of Ar($1s$) atoms when switching from argon to 17% Ar + He are twice. First, the e-impact collisional transfer rates between metastable and neighboring resonance states will be much reduced in the mixture, almost decoupling their respective densities. Second, the most frequent 3-body quenching collision will be:



To our knowledge, no experimental or theoretical value for the rate coefficient of this reaction has been reported in the literature. The quenching coefficient of Ar($1s_5$) metastable atoms by He must be smaller than by Ar because helium was used as carrier gas in the afterglow experiments of Jones *et al* for the study of argon metastable atoms reaction with different reactants.⁸² Also, the rate coefficient for the quenching of excited Ar* atoms by He was found to be smaller, or comparable to their quenching by argon.⁸³ In the present case of reactions 24 and 27, the 3rd collision partner (Ar or He) is only acting for the stabilization of the transient Ar₂^{*} excimer formed after Ar($1s$)-Ar encounter. Considering that the 3rd collision partner plays an identical kinetic role in both reactions, we will assume for reaction 27 a similar rate coefficient than in reaction 24. However, as the gas mixture contains only 17% of argon, the 3-body quenching frequencies of Ar($1s$) states will be 0.17 times the above calculated frequencies in pure argon discharge. Taking into account the gas density change

with the temperature (365 K in Ar and 335 K in He + 17% Ar plasmas), we end up with 3-body collision quenching frequencies ν_q of $2.0 \times 10^5 \text{ s}^{-1}$ and $1.0 \times 10^6 \text{ s}^{-1}$ for $1s_2$ and $1s_4$ states, respectively. However, in He + 17% Ar mixture, the effective radiative lifetimes predicted by the radiation trapping model^{79,80} remain unchanged, compared to the pure argon case. In fact, at atmospheric pressure the partial density of argon in the mixture is high enough for the spectral profile of the resonance lines 104.7 and 106.7 nm being still controlled by the resonance broadenings of their upper $1s_2$ and $1s_4$ states, respectively, and for the effective radiative lifetimes, predicted by the radiation trapping model, having reached their asymptotic highest values.^{79,80}

In He + 17% Ar discharge, the most remarkable difference between the density distribution profiles of atoms in the four $1s$ states, but also with the pure Ar case, is the much slower decay of the density of Ar($1s_2$) atoms toward the plasma center. In the middle of electrodes, the density of Ar($1s_2$) atoms is only 5 times smaller than its peak value at the sheath region but the relative change for metastable Ar($1s_5$) density is about 30 (Fig. 13). This peculiar behavior of Ar($1s_2$) atoms density in the He + 17% Ar gas mixture is attributed to the smallness of the 3-body quenching rate of the $1s_2$ state, which permits the spatial transport of the excitation in this state by radiation trapping phenomenon. To verify this assertion, a collisional radiative model, based on the random walk of resonance photon by Monte Carlo statistic was developed as discussed in Section II H and the results are discussed below.

D. Excitation transport by resonance radiation

Fig. 14 represents the measured and simulated densities of atoms in $1s_2$ and $1s_4$ states in the pure argon discharge. The simulation is performed as described in detail in Section II H. The peak amplitudes are normalized to 1 and, in the simulation, the plasma excitation zone of 0.14 mm wide was set between 0.2 and 0.34 mm from electrodes (positions ± 0.66 to ± 0.8 mm).

At the gap center, the simulated density of $1s_2$ atoms is larger than that of $1s_4$ atoms because the former being less exposed to the 3-body quenching collisions during their short radiative lifetime, the 104.8 nm photons can propagate farther from their production zone and create $1s_2$ atoms in the central part of the gap. However, the uncertainty level on measured densities in positions far from the sheaths does not permit an indisputable conclusion for the agreement between experimental and simulated density profiles. Nonetheless, the different behavior of $1s_2$ and $1s_4$ atoms as found in the experiment in the He + 17% Ar mixture is clearly reproduced by the model (Fig. 15). In the simulated profiles, the plasma excitation zone of 0.20 mm wide was set between 0.3 and 0.5 mm from electrodes (positions ± 0.5 to ± 0.7 mm). Thanks to the larger density of excited atoms in this discharge, the signal-to-noise ratio of the experimental data points is much better and a good agreement with simulated profiles is observed. It should be pointed out that with about 5 times smaller 3-body quenching rates in this plasma, compared to pure argon discharge,

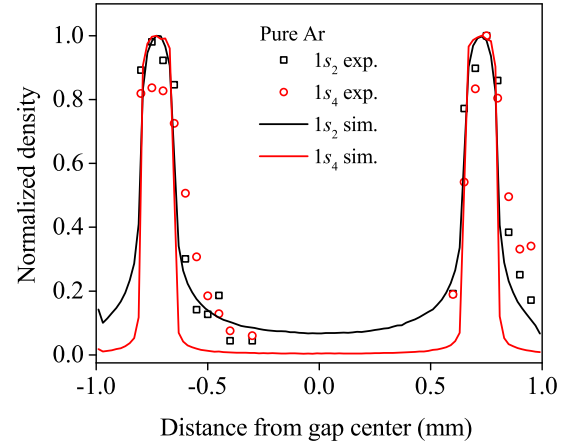


FIG. 14. Measured and simulated normalized densities of atoms in $1s_2$ and $1s_4$ resonant states in the pure Ar plasma.

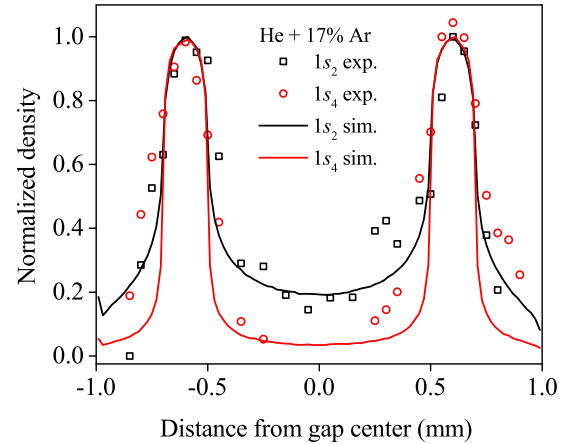


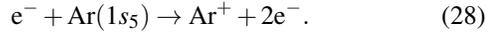
FIG. 15. Measured and simulated normalized densities of atoms in $1s_2$ and $1s_4$ resonant states in the He + 17% Ar plasma.

the resonance photons can diffuse farther from the sheath regions and transport the excitation in the resonance states to the central part of the plasma volume. We also note that the ratio between the quenching frequency (ν_q) and the radiative decay frequency ($1/\tau_{\text{rad}}$) being 20 times smaller in the mixture for $1s_2$ atoms than for $1s_4$ ones (3.8×10^{-4} and 7.6×10^{-3} , respectively), the excitation transport by 104.8 nm photons is more efficient than by 106.7 nm photons.

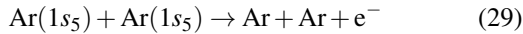
E. Comparison with He RF glow discharge

The RF glow discharges operated in He have been intensively studied both experimentally and theoretically,^{67,76,84} while a diffuse RF glow discharge in Ar has not been investigated in detail to date. Unlike glow discharges in He, the gas temperature is higher and the emission intensity is stronger in pure Ar discharge. The dominant mode of ionization in He

discharge is through Penning ionization of impurities present in the gas such as N_2 , O_2 or H_2O . However, the energy in the metastable state of Ar is too low to enable Penning ionization. Considering a Maxwellian EEDF, most ionization would occur from direct electron impact of ground-state Ar atoms with an ionization rate of $1.6 \times 10^{25} \text{ m}^{-3}\text{s}^{-1}$,³⁸ however, if the EEDF is non-Maxwellian, the dominant ionization mechanism for the estimated electron temperature of 2.1 eV from the continuum emission measurement needs to be stepwise ionization with an ionization rate of $1.0 \times 10^{23} \text{ m}^{-3}\text{s}^{-1}$.³⁸



Associative ionization,



with a rate coefficient of $6.4 \times 10^{-16} \text{ m}^3\text{s}^{-1}$,⁷⁷ has an ionization rate that is 2 orders of magnitude smaller than the stepwise ionization 28. A brief comparison of the measured plasma properties of Ar discharge reported in this paper with He RF glow discharge is summarized in Table VI.

IV. CONCLUSION

In this work, a radio frequency-driven capacitively coupled argon glow discharge at atmospheric pressure is investigated. We deduce the electron temperature and density by fitting the absolute intensity of the recorded emission spectrum with the stimulated spectrum of the neutral bremsstrahlung radiation. Using a non-Maxwellian EEDF, the time and space-averaged T_e and n_e of of 2.1 eV and $1.1 \times 10^{19} \text{ m}^{-3}$ were estimated, respectively, for pure Ar plasma. Using similar approach for a diffuse He RF discharge, a T_e of 3.5 eV and an n_e of $1.2 \times 10^{17} \text{ m}^{-3}$ were obtained.

We also have applied for the first time broadband absorption spectroscopy for the measurement of the space-resolved absolute density of atoms in metastable ($1s_5$ and $1s_3$) and resonant ($1s_4$ and $1s_2$) states of argon in a 2 mm wide plasma reactor running in pure argon or Ar/He mixture at atmospheric pressure. In all the discharge conditions, the density profiles of these excited atoms across the plasma gap showed features similar to the light emission profile of a glow RF discharge operated in the α -mode at atmospheric pressure. A maximum density of the order of 10^{18} m^{-3} was obtained for the $1s_5$ metastable atoms, while in the other metastable state ($1s_3$) and resonant states, $1s_4$ and $1s_2$, maximum densities were $\sim 2 \times 10^{17} \text{ m}^{-3}$, which occurred in the sheath region. The major production mechanisms of metastable atoms are the electron-impact excitation from the ground state and the dissociative electron-ion recombination of the Ar_2^+ ions. Their dominant loss mechanism is through the three-body collisional quenching with 2 ground state argon atoms, forming Ar_2^* excimer. Beside the above cited production and loss mechanisms, atoms in the resonance states are also lost by radiative

decay to the ground state, controlled by the resonance radiation trapping process in the optically thick medium. While the density of atoms in three $1s_5$, $1s_4$ and $1s_3$ states drops by factor 10 within 200 μm aside their production zone in the sheath region and becomes hardly detectable, the density of $1s_2$ resonance atoms in the center of the He + 17% Ar discharge is about 20% of its peak value in the sheath. This peculiar behavior is attributed to the smaller 3-body quenching rate coefficient of $1s_2$ atoms, compared to the 3 other $1s$ atoms and its shorter radiative lifetime, relative to that of the $1s_4$ state. This assertion is confirmed by comparing the measured density profiles of atoms in the resonance states to the density profiles calculated with a kinetic Monte Carlo statistic code of the random walk of the resonance photons in optically thick medium. A detailed comparison of the key plasma properties measured for both He and Ar RF glow discharges shows, for the same power density, significantly larger T_e for He compared to Ar, while the electron density is more than an order of magnitude higher in Ar than in helium.

ACKNOWLEDGMENTS

This work was supported by the US Department of Energy, Office of Science, Office of Fusion Energy Sciences General Plasma Science program under Award Number AT4010100 and DE-SC-0020232 and by the NSF grant under Award Number PHYS 1903151. GN gratefully acknowledges the Kermit and Ione Ebeltoft Interdisciplinary Doctoral Fellowship for 2018-19 and the Doctoral Dissertation Fellowship for 2019-20.

DATA AVAILABILITY

The data that support the findings of this study are available from the corresponding author upon reasonable request.

- ¹J. Han and M. C. Heaven, "Kinetics of optically pumped Ar metastables," *Optics Letters* **39**, 6541–6544 (2014).
- ²D. Emmons and D. Weeks, "Kinetics of high pressure argon-helium pulsed gas discharge," *Journal of Applied Physics* **121**, 203301 (2017).
- ³D. Emmons, D. Weeks, B. Eshel, and G. Perram, "Metastable Ar($1s_5$) density dependence on pressure and argon-helium mixture in a high pressure radio frequency dielectric barrier discharge," *Journal of Applied Physics* **123**, 043304 (2018).
- ⁴A. R. Hoskinson, J. Gregorío, J. Hopwood, K. Galbally-Kinney, S. J. Davis, and W. T. Rawlins, "Argon metastable production in argon-helium microplasmas," *Journal of Applied Physics* **119**, 233301 (2016).
- ⁵A. R. Hoskinson, J. Gregorío, J. Hopwood, K. L. Galbally-Kinney, S. J. Davis, and W. T. Rawlins, "Spatially resolved modeling and measurements of metastable argon atoms in argon-helium microplasmas," *Journal of Applied Physics* **121**, 153302 (2017).
- ⁶G. Isbary, G. Morfill, H. Schmidt, M. Georgi, K. Ramrath, J. Heinlin, S. Karrer, M. Landthaler, T. Shimizu, B. Steffes, *et al.*, "A first prospective randomized controlled trial to decrease bacterial load using cold atmospheric argon plasma on chronic wounds in patients," *British Journal of Dermatology* **163**, 78–82 (2010).
- ⁷C. Van Gils, S. Hofmann, B. Boekema, R. Brandenburg, and P. Brugge-geman, "Mechanisms of bacterial inactivation in the liquid phase induced by a remote RF cold atmospheric pressure plasma jet," *Journal of Physics D: Applied Physics* **46**, 175203 (2013).

TABLE VI. Comparison of RF glow discharges in He and Ar.

Parameter	He	Ar
Ionization	Penning ionization	Stepwise (metastable) ionization
Metastable atoms/molecules ^a	2^3S $((6.2 \pm 0.4) \times 10^{18} \text{ m}^{-3})$, $a^3\Sigma_u^+$ $((2.5 \pm 0.6) \times 10^{18} \text{ m}^{-3})$ ³¹	$1s_5$ $((6.9 \pm 0.4) \times 10^{17} \text{ m}^{-3})$, $1s_3$ $((1.13 \pm 0.12) \times 10^{17} \text{ m}^{-3})$
Resonant atoms ^a	–	$1s_4$ $((1.72 \pm 0.08) \times 10^{17} \text{ m}^{-3})$, $1s_2$ $((2.12 \pm 0.11) \times 10^{17} \text{ m}^{-3})$
Power density	38.6 Wcm^{-3}	37.2 Wcm^{-3}
Sheath width	$160 \pm 10 \mu\text{m}$ ^b $380 \pm 41 \mu\text{m}$ ^c	$170 \pm 10 \mu\text{m}$ ^b $180 \pm 9 \mu\text{m}$ ^c
RF mode	α -mode	α -mode
n_e	$(1.2 \pm 0.2) \times 10^{17} \text{ m}^{-3}$	$(1.1 \pm 0.7) \times 10^{19} \text{ m}^{-3}$
T_e	$(3.5 \pm 0.4) \text{ eV}$	$(2.1 \pm 0.3) \text{ eV}$

^a Maximum densities measured in the sheath region of the discharge.

^b From optical imaging using digital camera.

^c From equivalent electrical model.

- ⁸K. Wende, P. Williams, J. Dalluge, W. Van Gaens, H. Aboubakr, J. Bischof, T. Von Woedtke, S. M. Goyal, K.-D. Weltmann, A. Bogaerts, *et al.*, “Identification of the biologically active liquid chemistry induced by a nonthermal atmospheric pressure plasma jet,” *Biointerphases* **10**, 029518 (2015).
- ⁹S. Canulescu, J. Whitby, K. Fuhrer, M. Hohl, M. Gonin, T. Horvath, and J. Michler, “Potential analytical applications of negative ions from a pulsed radiofrequency glow discharge in argon,” *Journal of Analytical Atomic Spectrometry* **24**, 178–180 (2009).
- ¹⁰S. K. Øiseth, A. Krozer, B. Kasemo, and J. Lausmaa, “Surface modification of spin-coated high-density polyethylene films by argon and oxygen glow discharge plasma treatments,” *Applied Surface Science* **202**, 92–103 (2002).
- ¹¹N. Gomathi and S. Neogi, “Surface modification of polypropylene using argon plasma: Statistical optimization of the process variables,” *Applied Surface Science* **255**, 7590–7600 (2009).
- ¹²Z. Machala, K. Hensel, and Y. Akishev, *Plasma for bio-decontamination, medicine and food security* (Springer Science & Business Media, 2012).
- ¹³K. Stapelmann, O. Kylián, B. Denis, and F. Rossi, “On the application of inductively coupled plasma discharges sustained in Ar/O₂/N₂ ternary mixture for sterilization and decontamination of medical instruments,” *Journal of Physics D: Applied Physics* **41**, 192005 (2008).
- ¹⁴C. Hertwig, K. Reineke, J. Ehlbeck, D. Knorr, and O. Schlüter, “Decontamination of whole black pepper using different cold atmospheric pressure plasma applications,” *Food Control* **55**, 221–229 (2015).
- ¹⁵S. De Benedictis and G. Dilecce, “Energy transfers by long-lived species in glows and afterglows,” *Pure and Applied Chemistry* **74**, 317–326 (2002).
- ¹⁶A. Bogaerts, R. Gijbels, and J. Vlcek, “Collisional-radiative model for an argon glow discharge,” *Journal of Applied Physics* **84**, 121–136 (1998).
- ¹⁷S. Rauf and M. J. Kushner, “Argon metastable densities in radio frequency Ar, Ar/O₂ and Ar/CF₄ electrical discharges,” *Journal of Applied Physics* **82**, 2805–2813 (1997).
- ¹⁸X.-M. Zhu and Y.-K. Pu, “A simple collisional–radiative model for low-temperature argon discharges with pressure ranging from 1 Pa to atmospheric pressure: kinetics of Paschen 1s and 2p levels,” *Journal of Physics D: Applied Physics* **43**, 015204 (2009).
- ¹⁹A. Bogaerts and R. Gijbels, “Description of the argon-excited levels in a radio-frequency and direct current glow discharge,” *Spectrochimica Acta Part B: Atomic Spectroscopy* **55**, 263–278 (2000).
- ²⁰W. Van Gaens and A. Bogaerts, “Kinetic modelling for an atmospheric pressure argon plasma jet in humid air,” *Journal of Physics D: Applied Physics* **46**, 275201 (2013).
- ²¹K. Tachibana, “Excitation of the $1s_5$, $1s_4$, $1s_3$, and $1s_2$ levels of argon by low-energy electrons,” *Physical Review A* **34**, 1007 (1986).
- ²²B. Niermann, M. Böke, N. Sadeghi, and J. Winter, “Space resolved density measurements of argon and helium metastable atoms in radio-frequency generated He-Ar micro-plasmas,” *The European Physical Journal D* **60**, 489–495 (2010).
- ²³B. Eshel, C. A. Rice, and G. P. Perram, “Pressure broadening and shift rates for Ar(s–p) transitions observed in an Ar–He discharge,” *Journal of Quantitative Spectroscopy and Radiative Transfer* **179**, 40–50 (2016).
- ²⁴I. Stefanović, T. Kuschel, S. Schröter, and M. Böke, “Argon metastable dynamics and lifetimes in a direct current microdischarge,” *Journal of Applied Physics* **116**, 113302 (2014).
- ²⁵S. G. Belostotskiy, V. M. Donnelly, D. J. Economou, and N. Sadeghi, “Spatially resolved measurements of argon metastable ($1s_5$) density in a high pressure microdischarge using diode laser absorption spectroscopy,” *IEEE Transactions on Plasma Science* **37**, 852–858 (2009).
- ²⁶M. Schulze, A. Yanguas-Gil, A. Von Keudell, and P. Awakowicz, “A robust method to measure metastable and resonant state densities from emission spectra in argon and argon-diluted low pressure plasmas,” *Journal of Physics D: Applied Physics* **41**, 065206 (2008).
- ²⁷G. Hebner, “Spatially resolved, excited state densities and neutral and ion temperatures in inductively coupled argon plasmas,” *Journal of Applied Physics* **80**, 2624–2636 (1996).
- ²⁸E. Carbone, E. Van Veldhuizen, G. Kroesen, and N. Sadeghi, “Electron impact transfer rates between metastable and resonant states of argon investigated by laser pump–probe technique,” *Journal of Physics D: Applied Physics* **48**, 425201 (2015).
- ²⁹E. Carbone, S. Hübner, J. Van Der Mullen, G. Kroesen, and N. Sadeghi, “Determination of electron-impact transfer rate coefficients between argon $1s_2$ and $1s_3$ states by laser pump–probe technique,” *Journal of Physics D: Applied Physics* **46**, 415202 (2013).
- ³⁰J. Golda, F. Kogelheide, P. Awakowicz, and V. Schulz-von der Gathen, “Dissipated electrical power and electron density in an RF atmospheric pressure helium plasma jet,” *Plasma Sources Science and Technology* **28**, 095023 (2019).
- ³¹G. Nayak, N. Sadeghi, and P. Bruggeman, “He(2^3S_1) and He₂($a^3\Sigma_u^+$) metastables densities measured in an RF-driven helium plasma using broadband absorption spectroscopy,” *Plasma Sources Science and Technology* **28**, 125006 (2019).
- ³²G. Oinuma, G. Nayak, Y. Du, and P. J. Bruggeman, “Controlled plasma–droplet interactions: a quantitative study of OH transfer in plasma–liquid interaction,” *Plasma Sources Science and Technology* **29**, 095002 (2020).
- ³³S. Park, W. Choe, H. Kim, and J. Y. Park, “Continuum emission-based electron diagnostics for atmospheric pressure plasmas and characteristics of nanosecond-pulsed argon plasma jets,” *Plasma Sources Science and Technology* **24**, 034003 (2015).
- ³⁴S. Park, W. Choe, S. Youn Moon, and J. Park, “Electron density and temperature measurement by continuum radiation emitted from weakly ionized atmospheric pressure plasmas,” *Applied Physics Letters* **104**, 084103 (2014).
- ³⁵D. Hammer and L. Frommhold, “Polarization bremsstrahlung spectra of electron–rare-gas atom collisions at temperatures from 5 to 40 kK,” *Physical Review A* **64**, 024705 (2001).

- ³⁶A. Z. Akcasu and L. H. Wald, “Bremsstrahlung of slow electrons in neutral gases and free-free absorption of microwaves,” *The Physics of Fluids* **10**, 1327–1335 (1967).
- ³⁷K. T. A. L. Burm, “Continuum radiation in a high pressure argon–mercury lamp,” *Plasma Sources Science and Technology* **13**, 387 (2004).
- ³⁸G. Hagelaar and L. Pitchford, “Solving the Boltzmann equation to obtain electron transport coefficients and rate coefficients for fluid models,” *Plasma Sources Science and Technology* **14**, 722 (2005).
- ³⁹V. Kas’yanov and A. Starostin, “On the theory of bremsstrahlung of slow electrons on atoms,” *Soviet Physics JETP* **21**, 15 (1965).
- ⁴⁰“Phelps database,” <http://www.lxcat.net>, retrieved on June 17, 2020.
- ⁴¹L. Taghizadeh, A. Nikiforov, R. Morent, J. van der Mullen, and C. Leys, “Determination of the electron temperature of atmospheric pressure argon plasmas by absolute line intensities and a collisional radiative model,” *Plasma Processes and Polymers* **11**, 777–786 (2014).
- ⁴²Q. Xiong, A. Y. Nikiforov, M. A. González, C. Leys, and X. P. Lu, “Characterization of an atmospheric helium plasma jet by relative and absolute optical emission spectroscopy,” *Plasma Sources Science and Technology* **22**, 015011 (2012).
- ⁴³K. McKay, F. Iza, and M. Kong, “Excitation frequency effects on atmospheric-pressure helium RF microplasmas: plasma density, electron energy and plasma impedance,” *The European Physical Journal D* **60**, 497–503 (2010).
- ⁴⁴M. A. Lieberman and A. J. Lichtenberg, *Principles of plasma discharges and materials processing*, 2nd ed. (John Wiley & Sons, 2005).
- ⁴⁵P. Chabert and N. Braithwaite, *Physics of radio-frequency plasmas* (Cambridge University Press, 2011).
- ⁴⁶Y. P. Raizer, *Gas Discharge Physics* (Springer, 1991).
- ⁴⁷Y. Du, G. Nayak, G. Oinuma, Y. Ding, Z. Peng, and P. J. Bruggeman, “Emission considering self-absorption of OH to simultaneously obtain the OH density and gas temperature: validation, non-equilibrium effects and limitations,” *Plasma Sources Science and Technology* **26**, 095007 (2017).
- ⁴⁸P. Bruggeman, G. Cunge, and N. Sadeghi, “Absolute OH density measurements by broadband UV absorption in diffuse atmospheric-pressure He–H₂O rf glow discharges,” *Plasma Sources Science and Technology* **21**, 035019 (2012).
- ⁴⁹M. Kogelschatz, G. Cunge, and N. Sadeghi, “Identification of halogen containing radicals in silicon etching plasmas and density measurement by UV broad band absorption spectroscopy,” *Journal of Physics D: Applied Physics* **37**, 1954 (2004).
- ⁵⁰Y. Du, G. Nayak, G. Oinuma, Z. Peng, and P. J. Bruggeman, “Effect of water vapor on plasma morphology, OH and H₂O₂ production in He and Ar atmospheric pressure dielectric barrier discharges,” *Journal of Physics D: Applied Physics* **50**, 145201 (2017).
- ⁵¹A. Kramida, Y. Ralchenko, J. Reader, and NIST ASD Team, NIST Atomic Spectra Database (ver. 5.7.1), [Online]. Available: <https://physics.nist.gov/asd> [2019, October 20]. National Institute of Standards and Technology, Gaithersburg, MD. (2019).
- ⁵²H. L. Anderson, *A physicist’s desk reference*, 2nd ed. (New York: American Institute of Physics (AIP), 1989).
- ⁵³C. Lee, D. Camm, and G. Copley, “Van der Waals broadening of argon absorption lines,” *Journal of Quantitative Spectroscopy and Radiative Transfer* **15**, 211–216 (1975).
- ⁵⁴J. Rosato, Y. Marandet, D. Reiter, and R. Stamm, “Development of a hybrid kinetic–fluid model for line radiation transport in magnetic fusion plasmas,” *High Energy Density Physics* **22**, 73–76 (2017).
- ⁵⁵J. Rosato, “Derivation of a transport equation for line radiation using the Wigner Phase Space Formalism,” *Journal of Computational and Theoretical Transport* **47**, 18–27 (2018).
- ⁵⁶J. Spanier and E. M. Gelbard, *Monte Carlo principles and neutron transport problems* (Courier Corporation, 2008).
- ⁵⁷C. Yamabe, S. Buckman, and A. Phelps, “Measurement of free-free emission from low-energy-electron collisions with Ar,” *Physical Review A* **27**, 1345 (1983).
- ⁵⁸I. Denysenko, H. Kersten, and N. Azarenkov, “Electron energy distribution in a dusty plasma: analytical approach,” *Physical Review E* **92**, 033102 (2015).
- ⁵⁹V. I. Kolobov and V. A. Godyak, “Nonlocal electron kinetics in collisional gas discharge plasmas,” *IEEE Transactions on Plasma Science* **23**, 503–531 (1995).
- ⁶⁰J. Golda, J. Held, and V. Schulz-von der Gathen, “Comparison of electron heating and energy loss mechanisms in an RF plasma jet operated in argon and helium,” *Plasma Sources Science and Technology* **29**, 025014 (2020).
- ⁶¹J. Gudmundsson, “Technical Report RH-21-2002 Science Institute,” University of Iceland (2002).
- ⁶²D. Levko and L. L. Raja, “Electron kinetics in atmospheric-pressure argon and nitrogen microwave microdischarges,” *Journal of Applied Physics* **119**, 163303 (2016).
- ⁶³M. Atanasova, A. Sobota, W. Brok, G. Degrez, and J. Van Der Mullen, “Driving frequency dependence of capacitively coupled plasmas in atmospheric argon,” *Journal of Physics D: Applied Physics* **45**, 335201 (2012).
- ⁶⁴M. Atanasova, E. Carbone, D. Mihailova, E. Benova, G. Degrez, and J. Van Der Mullen, “Modelling of an RF plasma shower,” *Journal of Physics D: Applied Physics* **45**, 145202 (2012).
- ⁶⁵M. Moravej, X. Yang, G. Nowling, J. Chang, R. Hicks, and S. Babayan, “Physics of high-pressure helium and argon radio-frequency plasmas,” *Journal of Applied Physics* **96**, 7011–7017 (2004).
- ⁶⁶N. Balcon, G. Hagelaar, and J. Boeuf, “Numerical model of an argon atmospheric pressure RF discharge,” *IEEE Transactions on Plasma Science* **36**, 2782–2787 (2008).
- ⁶⁷J. Shi and M. Kong, “Mechanisms of the α and γ modes in radio-frequency atmospheric glow discharges,” *Journal of Applied Physics* **97**, 023306 (2005).
- ⁶⁸Y. B. Golubovskii, V. Maiorov, J. Behnke, and J. Behnke, “Modelling of the homogeneous barrier discharge in helium at atmospheric pressure,” *Journal of Physics D: Applied Physics* **36**, 39 (2002).
- ⁶⁹Y. Wang and D. Wang, “Influence of impurities on the uniform atmospheric-pressure discharge in helium,” *Physics of Plasmas* **12**, 023503 (2005).
- ⁷⁰G. Copley and D. Camm, “Pressure broadening and shift of argon emission lines,” *Journal of Quantitative Spectroscopy and Radiative Transfer* **14**, 899–907 (1974).
- ⁷¹D. Aeschliman, R. Hill, and D. Evans, “Collisional broadening and shift of neutral argon spectral lines,” *Physical Review A* **14**, 1421 (1976).
- ⁷²D. Stacey and J. Vaughan, “Pressure broadening and oscillator strengths in argon,” *Physics Letters* **11**, 105–106 (1964).
- ⁷³P. Moussounda and P. Ranson, “Pressure broadening of argon lines emitted by a high-pressure microwave discharge (Surfatron),” *Journal of Physics B: Atomic and Molecular Physics* **20**, 949 (1987).
- ⁷⁴O. Vallee, P. Ranson, and J. Chapelle, “Measurements of broadening of argon lines and oscillator strengths of resonance lines,” *Journal of Quantitative Spectroscopy and Radiative Transfer* **18**, 327–336 (1977).
- ⁷⁵N. Konjević, A. Lesage, J. R. Fuhr, and W. L. Wiese, “Experimental Stark widths and shifts for spectral lines of neutral and ionized atoms (a critical review of selected data for the period 1989 through 2000),” *Journal of Physical and Chemical Reference Data* **31**, 819–927 (2002).
- ⁷⁶T. Gans, C. C. Lin, V. Schulz-Von Der Gathen, and H. Döbele, “Phase-resolved emission spectroscopy of a hydrogen rf discharge for the determination of quenching coefficients,” *Physical Review A* **67**, 012707 (2003).
- ⁷⁷J. T. Gudmundsson and E. Thorsteinnsson, “Oxygen discharges diluted with argon: dissociation processes,” *Plasma Sources Science and Technology* **16**, 399 (2007).
- ⁷⁸J. Kolts and D. Setser, “Decay rates of Ar($4s, ^3P_2$), Ar($4s', ^3P_0$), Kr($5s, ^3P_2$), and Xe($6s, ^3P_2$) atoms in argon,” *The Journal of Chemical Physics* **68**, 4848–4859 (1978).
- ⁷⁹T. Holstein, “Imprisonment of resonance radiation in gases,” *Physical Review* **72**, 1212 (1947).
- ⁸⁰T. Holstein, “Imprisonment of resonance radiation in gases. II,” *Physical Review* **83**, 1159 (1951).
- ⁸¹P. Walsh, “Effect of simultaneous Doppler and collision broadening and of hyperfine structure on the imprisonment of resonance radiation,” *Physical Review* **116**, 511 (1959).
- ⁸²M. T. Jones, T. Dreiling, D. Setser, and R. N. McDonald, “Branching fractions for penning ionization in quenching of He(2^3S), Ar($^3P_{2,0}$), and Ne($^3P_{2,0}$) atoms,” *The Journal of Physical Chemistry* **89**, 4501–4517 (1985).
- ⁸³N. Sadeghi, D. Setser, A. Francis, U. Czarnetzki, and H. Döbele, “Quenching rate constants for reactions of Ar($4p\ ^1[1/2]_0$), $4p\ [1/2]_0$, $4p\ [3/2]_2$, and $4p\ [5/2]_2$) atoms with 22 reagent gases,” *The Journal of Chemical Physics* **115**, 3144–3154 (2001).

⁸⁴J. Park, I. Henins, H. Herrmann, G. Selwyn, and R. Hicks, "Discharge phenomena of an atmospheric pressure radio-frequency capacitive plasma source," *Journal of Applied Physics* **89**, 20–28 (2001).